Earth Planet. Sci. Lett. 626 (2024) 118515

Contents lists available at ScienceDirect

Earth and Planetary Science Letters

journal homepage: www.elsevier.com/locate/epsl

Injection-induced fault slip and associated seismicity in the lab: Insights from source mechanisms, local stress states and fault geometry

Lei Wang [a,*], Grzegorz Kwiatek [a], Marco Bohnhoff [a,b], Erik Rybacki [a], Georg Dresen [a,c]

[a] Helmholtz Centre Potsdam, GFZ German Research Centre for Geosciences, Potsdam, Germany
[b] Department of Earth Sciences, Free University Berlin, Berlin, Germany
[c] Institute of Earth and Environmental Science, University of Potsdam, Potsdam, Germany

ARTICLE INFO

Editor: Dr. R. Bendick

Keywords:
Injection-induced seismicity
Acoustic emission
Fault roughness
Source mechanism
Gutenberg–Richter *b*-value
On fault and off-fault seismicity

ABSTRACT

Probing source mechanisms of natural and induced earthquakes is a powerful tool to unveil associated rupture kinematics. The source processes of failure and slip instability driven by stress loading are affected by fault geometry, but the source ruptures of injection-induced seismicity in relation to fault structures and local stress states remain poorly understood. We have conducted a series of fault reactivation and slip experiments on sandstone samples containing faults with different surface roughness (smooth saw-cut fault and fractured rough fault). We impose progressive fluid injection to induce fault slip, and simultaneously monitor the associated acoustic emission (AE) activity. Using high-resolution AE recordings, we perform full moment tensor inversion of all located AE sources, and investigate the changes of AE source characteristics associated with induced fault slip and their relation to fault roughness. For the complex and rough fault, we observe significant non-double-couple components of AE sources and a high degree of focal mechanism heterogeneity. The temporal changes of AE mechanisms associated with injection-induced fault slip on the smooth fault reveal increasing proportions of double-couple components and decreasing variability of AE focal mechanisms when approaching the onset of slip events. The observed inconsistency between the nodal planes of AE sources and the macroscopic fault plane orientation is attributed to the development of secondary fracture networks surrounding the principal slip surface. We analyze changes in the magnitude-frequency characteristics and source mechanisms of AEs with fault-normal distance, showing that for the smooth (mature) fault, Gutenberg–Richter *b*-value of on-fault seismicity is lower and focal mechanisms are less heterogeneous, compared to off-fault seismicity. Our results emphasize the important role of roughness-related changes in local fault geometry and associated stress heterogeneity for source mechanisms and rupture kinematics of injection-induced seismicity.

1. Introduction

Fluid-induced earthquakes associated with anthropogenic activity have been documented in geothermal reservoir production, wastewater disposal and CO_2 sequestration (Ellsworth, 2013; Schultz et al., 2020). Fault reactivation and associated earthquakes can be attributed to increased fluid pressure acting on the fault plane, poroelastic stress changes and/or shear stress transfer through aseismic slip (Ellsworth, 2013; Guglielmi et al., 2015; Schultz et al., 2020). Natural faults and fractures typically display non- planar geometry, and fault surfaces exposed in outcrops reveal predominantly self-affine roughness characteristics over a wide range of length scales (Brodsky et al., 2016; Candela et al., 2012; Power et al., 1987; Power and Tullis, 1991; Renard et al., 2013). Fault geometry and roughness have been shown to cause stress and strength heterogeneity in space (Brown and Scholz, 1985; Chester and Chester, 2000; Dieterich and Smith, 2009; Fang and Dunham, 2013; Zielke et al., 2017), also to control distribution of earthquake hypocenters and magnitudes, stress drops, and source parameters (Allam et al., 2019; Cattania and Segall, 2021; Tal and Hager, 2018; Zielke et al., 2017).

Analysis of source mechanisms of tectonic and induced earthquakes allows constraining the amount of volumetric and shear strain in the seismic source. Also, stress tensor inversion allows estimating orientation and stress conditions surrounding reactivated faults. The inverted full moment tensor (FMT) may be decomposed into isotropic (ISO), compensated linear vector dipole (CLVD), and double-couple (DC)

* Corresponding author.
E-mail address: wanglei@gfz-potsdam.de (L. Wang).

https://doi.org/10.1016/j.epsl.2023.118515
Received 28 July 2023; Received in revised form 17 November 2023; Accepted 21 November 2023
Available online 9 December 2023

components (Knopoff and Randall, 1970; Vavryčuk, 2001). The ISO component quantifies volumetric change in the seismic source. Tensile opening is represented by positive ISO values, whereas negative ISO values indicate crack closure/collapse. The remaining two components of the moment tensor characterize deviatoric (non-volumetric) deformation. The DC represents pure shear motion along two possible nodal planes characterized by strike, dip, and rake (Julian et al., 1998; Miller et al., 1998). The ambiguity in selecting a nodal plane can be resolved using rupture directivity (e.g., Holmgren et al., 2023) or by considering the nodal plane most likely to fail in a defined stress field (e.g., Moeck et al., 2009; Vavryčuk, 2014). The CLVD represents motion away (if positive) or toward (if negative) the earthquake source with no net volumetric change, with complex interpretation (Frohlich, 1994; Julian et al., 1998). Significant non-DC components of fluid-induced seismic events have been reported from hydraulic fracturing in gas-bearing sediments and geothermal reservoirs (Cuenot et al., 2006; Martínez-Garzón et al., 2017; Šílený et al., 2009; Zhang et al., 2016). These are typically interpreted as a signature of fracture opening/closure associated with fluid injection/extraction operations. In contrast, some induced earthquakes accompanying injections into granitic geothermal reservoirs occurred as a consequence of pure shear failure along pre-existing fractures favorably oriented with respect to the local stress field (Fehler, 1989; Horálek et al., 2010). Source mechanisms of fluid-induced seismicity from four representative sites globally revealed comparable contribution of non-DC components from induced and tectonic earthquakes (Wang et al., 2018). The authors concluded that complex fault architectures and fracture networks likely dominate source mechanisms.

In addition to the field scale, FMT inversion has been applied to the analysis of grain-scale acoustic emission (AE) events associated with micro-fracturing and damage production during laboratory rock deformation experiments performed at well-defined boundary conditions (Blanke et al., 2020; Goebel et al., 2017; Graham et al., 2010; Kwiatek et al., 2014b; McLaskey and Lockner, 2014; Sellers et al., 2003; Thompson et al., 2009, 2005). AEs provide important insights into the development and coalescence of microfractures and damage, leading to dynamic failure. The analysis of AE source characteristics at the microscale may allow to better understand kinematics of natural earthquakes. For granite samples with smooth faults, large AEs had predominantly DC focal mechanisms while small AEs exhibited significant non-DC components (Kwiatek et al., 2014b; McLaskey and Lockner, 2014; Thompson et al., 2005). Stick-slip events on naturally fractured laboratory faults indicated substantial shear-enhanced compaction within a relatively broad damage zone during the inter-slip and post-slip periods of stick-slip events (Kwiatek et al., 2014b). In contrast to smooth faults, focal mechanisms of AEs on rough faults are more heterogeneous (Goebel et al., 2017; Thompson et al., 2009), due to stress field heterogeneity within the fault zones. It has been suggested that naturally fractured faults in laboratory specimens may correspond to complex fault systems on the field scale (Thompson et al., 2009). Premonitory AEs preceding dynamic instability also revealed a complex preparation and nucleation process (Dresen et al., 2020; Guérin-Marthe et al., 2023; McLaskey and Lockner, 2014; Thompson et al., 2005), controlled by heterogeneity of stress and fault surface conditions. Moreover, laboratory AEs shed light on the important role of seismic events with significant compaction components affecting aftershock triggering during rock fracture (Davidsen et al., 2021). However, to our knowledge source mechanisms and rupture kinematics of fluid-induced earthquakes in laboratory experiments and their relation to fault geometry and stress states have not been reported yet.

In this work, we present a detailed analysis of recorded AE activity associated with injection-induced slip on the laboratory faults. We performed a series of injection-induced fault slip experiments on quartz-rich sandstone samples containing faults with varying surface roughness (a polished saw-cut fault vs. naturally fractured rough faults). Based on AE-derived moment tensor solutions, we studied the effect of fault geometry and stress heterogeneity on spatiotemporal characteristics of AE source mechanisms. The kinematics of microscale slip derived from AE sources such as nodal planes and local slip vectors were compared with the macroscopic fault slip behavior. We also constrained the statistical characteristics of on-fault and off-fault seismicity in relation to fault geometry and stress states.

2. Experimental setup

2.1. Starting materials

As sample material we used Bentheim sandstone, a homogeneous and isotropic porous rock. It is composed of 97 % well-rounded quartz grains with diameter of 0.20–0.33 mm (Wang et al., 2020a, 2021). The sandstone has a high initial porosity (23.3 %) and a high permeability (10^{-12} m^2), resulting in a characteristic diffusion time on the order of milliseconds and thus rapid fluid pressure equilibrium across the whole sample during the fluid pressurization process (Wang et al., 2020b, 2021).

At a constant confining pressure of 35 MPa, we used a triaxial deformation apparatus to run fluid injection experiments on three cylindrical samples of Bentheim sandstone with geometry of 50 mm (diameter) × 100 mm (length). One sample contained a sawcut fault and two samples were cut by fractured rough faults. The three faults were all oriented at ϕ=30° to the cylinder axis (Fig. 1a). For the smooth sawcut fault, the scanned surface topography using a 3D optical profilometer (Keyence VR3200) gave a root-mean-square height of $h_{rms} \approx 0.044$ mm (Fig. 1b). To generate a naturally rough fault, we used a thin cutting disc to prepare an inclined circumferential notch (1.5 mm depth and 0.5 mm width) with an orientation of 30° to the cylinder axis. The prefabricated circumferential thin notch filled with low-friction Teflon sheets provided a guide for fracture propagation and coalescence in a triaxial compression test where the axial stress was increased until failure using a constant displacement rate of 1 μm/s at room temperature and effective confining pressure of 25 MPa, resulting in the formation of a naturally rough fracture (fault) surface. To test reproducibility of the experiments performed on fractured rough faults, we conducted two experiments on two individual fractured samples (hereafter named rough fault #1 and rough fault #2, respectively). For rough fault #1 and rough fault #2, the root-mean-square roughness was measured to be $h_{rms} \approx 1.50$ mm and 0.82 mm, respectively (Fig. 1c and Supplementary Fig. S1).

2.2. Experimental procedures

We performed triaxial deformation tests in an MTS loading frame (stiffness of ~650 kN/mm) equipped with a pore pressure system and AE recording system (see Supplementary Fig. S2 for details). At room temperature, the experiments were performed on saw-cut or fractured samples contained in a rubber jacket to prevent intrusion of the confining oil. The samples were first hydrostatically loaded up to 35 MPa (i.e., σ_3 was increased to 35 MPa) while the fluid pressure (p) was kept constant at 5 MPa. Then, the axial stress (σ_1) was increased using a constant load point velocity of 1 μm/s to obtain the steady-state shear strength (τ_{ss}) resolved on the fault interface. Subsequently, the axial stress was reduced slowly until the calculated shear stress along the fault interface equaled about $0.92\tau_{ss}$ for smooth fault and rough fault #1 and $0.86\tau_{ss}$ for rough fault #2, respectively. This gave initial effective normal and shear stresses of 50.1 MPa and 34.0 MPa for the saw-cut fault, 53.0 MPa and 39.5 MPa for the rough fault #1, and 49.6 MPa and 33.5 MPa for the rough fault #2, respectively (see Figs. 2a, 3a and Supplementary Fig. S7a). The similar initial stress levels before fluid injection among the three experiments indicated that stored elastic energy prior to induced slip was similar. Next, the position of the axial loading piston was kept constant, and we injected water from the bottom

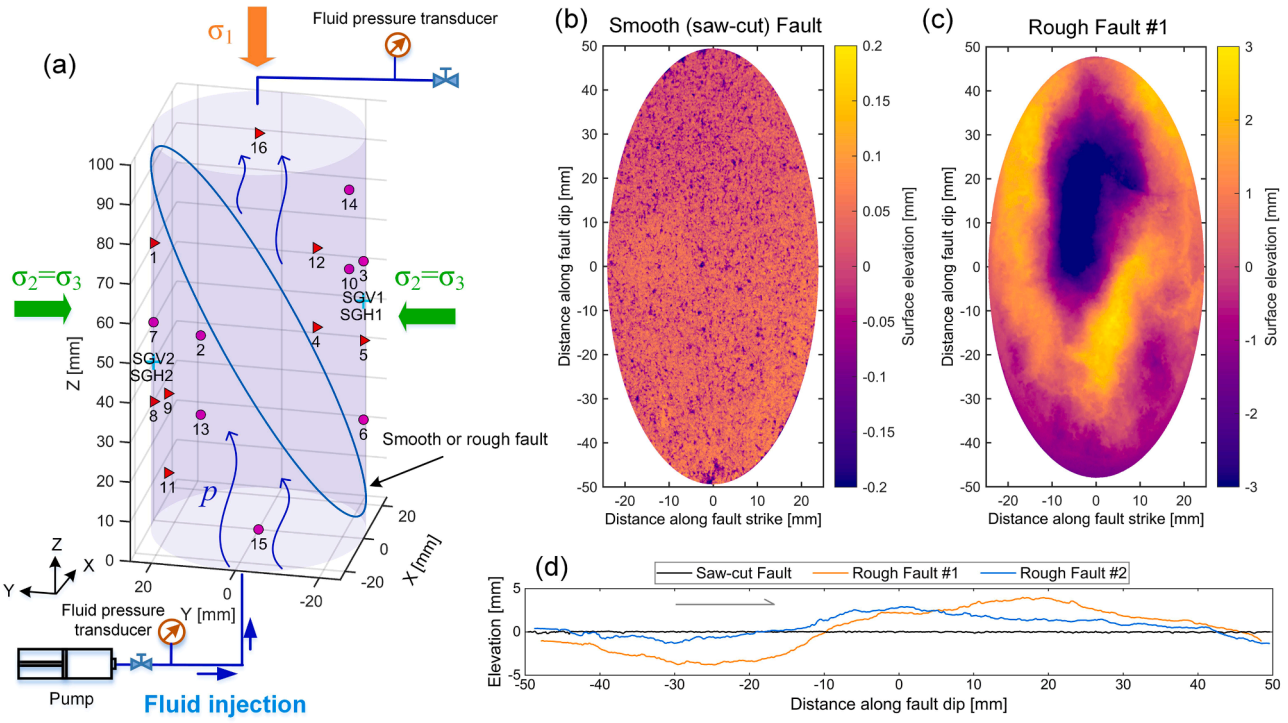

Fig. 1. (a) Experimental setup of fluid injection tests on cylindrical samples (50 × 100 mm) inducing fault reactivation. The permeable quartz-rich sandstone samples contain inclined smooth or rough faults with orientation of 30° relative to the vertical axis loaded in triaxial compression ($\sigma_1 > \sigma_2 = \sigma_3$, compression is positive). The inclined circumferential blue curve delineates the outer boundary of the laboratory fault. Red triangles and magenta circles denote positions of piezoelectric transducers (PZTs). Red triangles mark PZTs that periodically send ultrasonic transmission signals that are recorded by remaining sensors, used for periodic updates of the velocity model. Two vertical strain gages (SGV1 and SGV2) and two horizontal strain gages (SGH1 and SGH2) are attached at the center of two fault blocks for measuring deformation of the rock matrix. Fluid is injected from the bottom end of sample and the upper end of sample is isolated, resulting in undrained conditions. Real-time fluid pressures are simultaneously recorded using two pore pressure transducers at both ends of samples. (b-c) Surface elevation of the lower rock block for the smooth (saw-cut) and rough fault #1, respectively. (d) The surface profiles along fault up-dip direction (i.e., the major axis of fault ellipse) of the saw-cut and two rough faults (not to scale). The gray arrow gives the slip direction of the lower rock block relative to its counterpart.

end of the sample to induce slip at undrained conditions (Fig. 1a). We used a six-stage fluid injection protocol in which fluid pressure was increased stepwise from 5 MPa to 29 MPa with a pressurization rate of 2 MPa/min. In each stage, a duration of 10 min was composed of a ramp phase lasting for 2 min (4 MPa fluid pressure increment) and a subsequent plateau phase at constant p for 8 min. Throughout the experiment, mechanical and hydraulic data were synchronously recorded at a sampling rate of 10 Hz.

2.3. Strain and stress measurements

During the experiments, we measured the deformation and mechanical properties (Young's modulus and Poisson's ratio) of the rock matrix using two pairs of orthogonal strain gages (two vertical gages SGV1 and SGV2 and two horizontal gages SGH1 and SGH2) glued directly at the center of two sample parts (Fig. 1a).

We used an internal load cell to measure the axial stress (σ_1). The sample-averaged (macroscopic) shear stress (τ) and the effective normal stress (σ_n') resolved on the fault plane (compressive stress is positive), respectively, can be given by $\tau = (\sigma_1 - \sigma_3)\sin\phi\cos\phi$ and $\sigma_n' = (\sigma_3 - p) + (\sigma_1 - \sigma_3)\sin^2\phi$. We corrected for contact area reduction between two blocks due to relative slip (Wang et al., 2020c). Fault slip (s) can be estimated by $s = (\Delta l_{LVDT} - \Delta l_{machine} - \Delta l_{rock})/\cos\phi$ where Δl_{LVDT} is the total axial displacement measured by an external linear-variable displacement transducer (LVDT), $\Delta l_{machine}$ is the axial deformation of the loading machine and Δl_{rock} is the axial deformation of the rock matrix calculated from the mean axial strain of two vertical strain gages (SGV1 and SGV2), respectively. The average slip velocity was then obtained as time derivative of slip displacement.

2.4. Acoustic emission (AE) monitoring

AE activity was recorded using 16 one-component piezoelectric transducers (PZTs) (resonant frequency 1 MHz) attached directly to the sample surfaces, enabling optimum azimuthal coverage of AE events (Fig. 1a). Event waveforms were recorded in a triggered mode at 10 MHz sampling frequency (see Supplementary Fig. S2 for details). P-wave onsets times and first P-wave amplitudes of AE waveforms were picked using a combined Akaike information criterion and convolutional neural network method (Dresen et al., 2020; Guérin-Marthe et al., 2023; Wang et al., 2020c). We also actively measured ultrasonic P-wave velocities along different travelling traces every 10 s (Fig. 1a), which provided a time-dependent quasi-anisotropic velocity model composed of five horizontal layers and one vertical layer. Combining with the updated velocity model, at least 8 available P-wave onset times of recorded high signal-to-noise ratio waveforms were inverted to locate AE hypocenters using a grid-search method and simplex optimization algorithm by minimizing the least absolute value of arrival time errors, resulting in location accuracy ±2 mm (Dresen et al., 2020; Guérin-Marthe et al., 2023; Wang et al., 2020c). During the fluid injection experiments, AE recordings did not indicate saturation, and only a few large AEs may have clipped waveforms but not for the first P-wave amplitudes.

3. Methods

3.1. Gutenberg–Richter b-value

The relative AE magnitude M_{AE} may be estimated using (Zang et al., 1998)

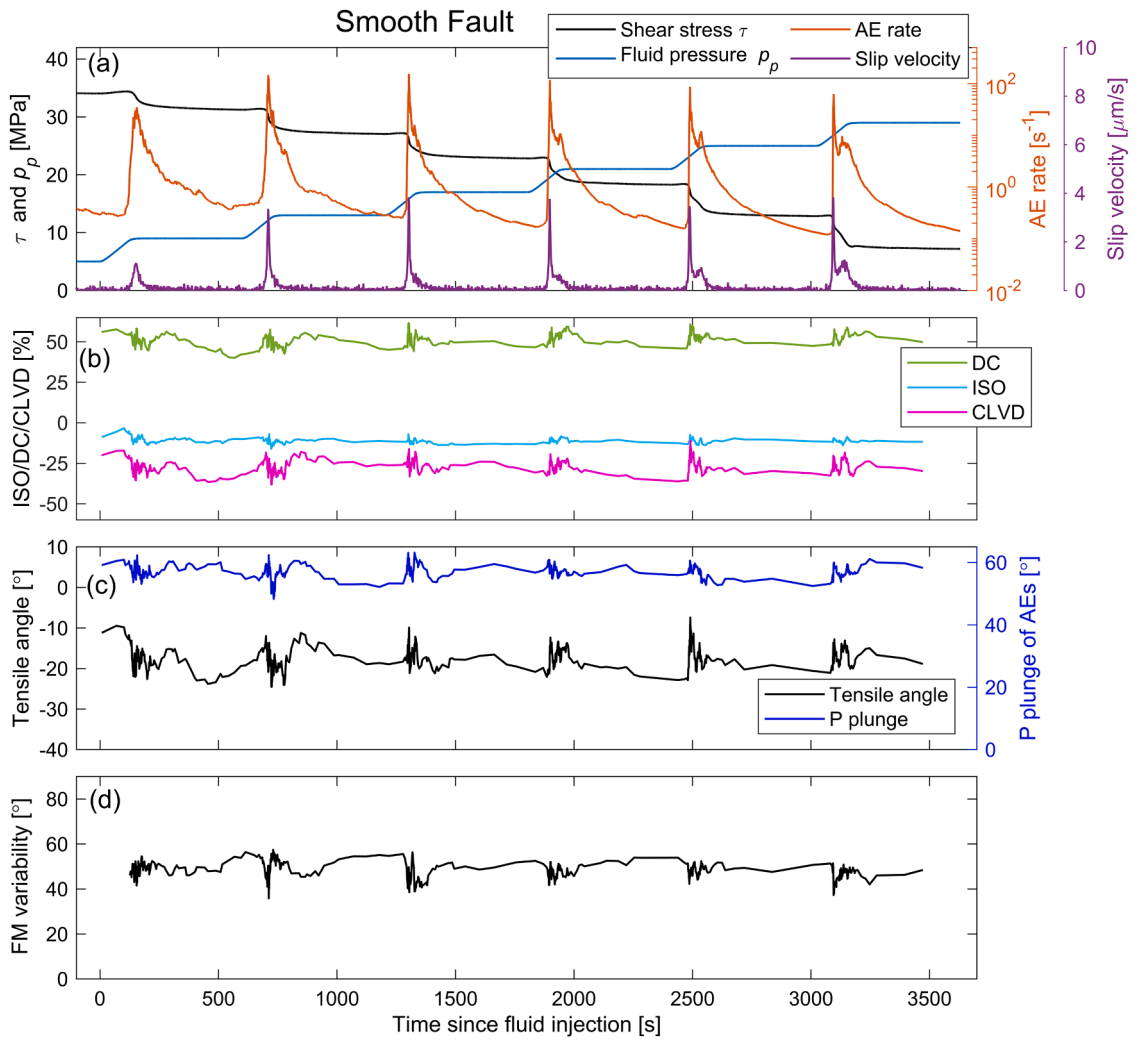

Fig. 2. (a) Temporal changes of injection-induced shear stress, fault slip rate, and AE rate recorded in the experiment on the smooth (saw-cut) fault starting from the moment of fluid injection into the fault. Prior to fluid injection, the initial effective normal and shear stresses acting on the smooth fault are 50.1 MPa and 34.0 MPa, respectively. (b-d) Temporal changes of AE-derived parameters including DC, ISO, and CLVD percentages, P-axis plunge, tensile angle and focal mechanism (FM) variability. To calculate temporal changes in (b-d), we use a moving window containing 50 AEs with a step of 5 AEs to calculate the mean values.

$$M_{\mathrm{AE}} = \log_{10}\sqrt{\frac{1}{n}\sum_{i=1}^{n}(U_i R_i)^2} \tag{1}$$

where U_i and R_i are the first P-wave amplitude and source-receiver distance for the ith sensor, respectively.

Provided that the frequency-magnitude distribution of a given group of AE events follows the Gutenberg–Richter power law relation, we may estimate the b-value using a maximum likelihood approach (Shi and Bolt, 1982):

$$b = \log_{10}(e) \,/\, (\overline{M} - M_c), \tag{2}$$

where M_c is the magnitude of completeness, and $\overline{M}$ is the mean magnitude of AEs that are above M_c. During the period of fluid injection, the AE catalogues (time, location and AE magnitude) for the saw-cut fault, rough fault #1 and rough fault #2 contained 3983, 7627 and 6390 events, respectively. For all AE catalogues in each experiment, we performed a correction for the AE magnitude histogram with a bin width of 0.01 and used the goodness of fit at 90 % level to estimate M_c (e.g., Wiemer and Wyss, 2002, 1997), leading to M_c=1.82, 1.86 and 1.77 for the saw-cut fault, rough fault #1 and rough fault #2, respectively (Supplementary Figs. S3–S5). The standard error (δ_b) of b-value can be estimated using the formulation by Shi and Bolt (1982):

$$\delta b = 2.3b^2\sqrt{\frac{\sum_{i=1}^{N}(M_i - \overline{M})^2}{N(N-1)}} \tag{3}$$

where M_i is the magnitude of ith AE event above M_c.

3.2. Full moment tensor of AE sources and derived parameters

Full moment tensor (FMT) inversion of laboratory AE events is sensitive to data quality, site effects and sensor characteristics, etc. Only AE events with $n \geq 12$ best available signal-to-noise ratio P-wave amplitudes were considered for FMT inversion. We corrected the first P-wave amplitudes for coupling quality of AE sensors and incidence angle (Kwiatek et al., 2014a). Following a point-source approximation, we used the hybridMT software (Kwiatek et al., 2016) to invert the symmetric second-rank (3 × 3) M_{ij} with six independent moment tensor elements for an individual AE event based on the corrected first P-wave amplitudes recorded by each PZT. We then evaluated uncertainties of the estimated FMT solutions using two parameters. First, we adopted normalized root-mean-square deviation (NRMSD) between theoretical U_i^{th} and observed U_i^{obs} of P-wave amplitudes (Stierle et al., 2016), as given by NRMSD $= \sqrt{\sum_{i=1}^{n}(U_i^{obs} - U_i^{th})^2 / \sum_{i=1}^{n}(U_i^{obs})^2}$. Second, we also

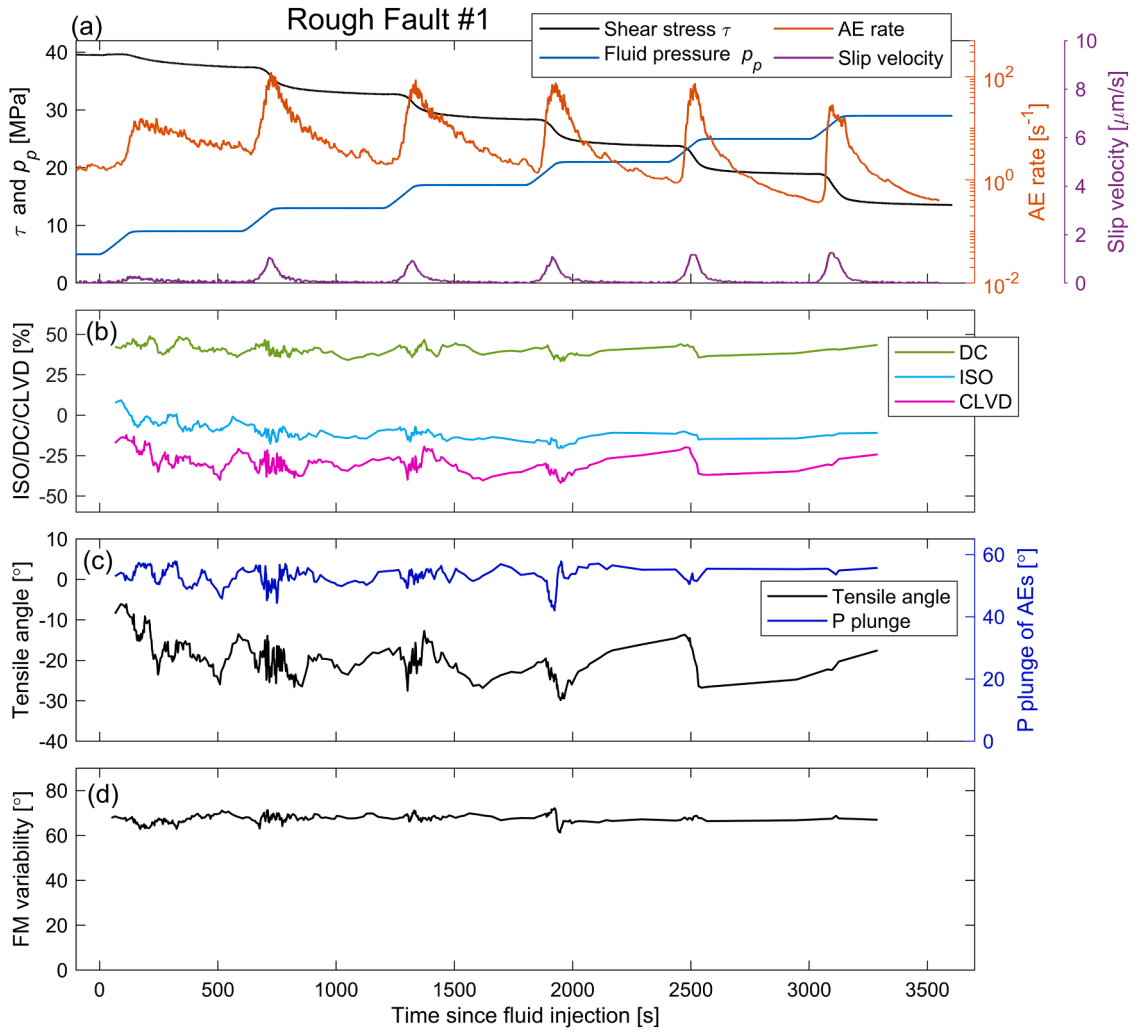

Fig. 3. (a) Temporal changes of injection-induced shear stress, fault slip rate, and AE rate recorded in the experiment on the rough fault #1 starting from the moment of fluid injection into the fault. Prior to fluid injection, the initial effective normal and shear stresses acting on the rough fault #1 are 53.0 MPa and 39.5 MPa, respectively. (b-d) Temporal changes of AE-derived parameters including DC, ISO, and CLVD percentages, P-axis plunge, tensile angle and focal mechanism (FM) variability. To calculate temporal changes in (b-d), we use a moving window containing 50 AEs with a step of 5 AEs to calculate the mean values.

used the scaled maximum error of the moment tensor components (MAXC) as a quality constraint. That is defined as the square root of the maximum diagonal element C_{ii} of the 6 × 6 covariance matrix of the six independent moment tensor elements normalized by the scalar seismic moment M_0 (i.e., MAXC=max($\sqrt{C_{ii}}$)/M_0). The inverted FMTs of most AE sources commonly had NRMSD < 0.8 and MAXC< 0.2 in our experiments (Supplementary Fig. S6). We assumed high-resolution FMTs satisfying both NRMSD < 0.5 and MAXC < 0.05, which were chosen for subsequent analysis.

The accepted FMTs were decomposed into ISO, CLDV, and DC components following the standard FMT decomposition scheme (Vavryčuk, 2001). In addition to percentages of ISO, CLVD, and DC components (|%ISO| + |%CLVD|+%DC= 100%), we extracted orientations of the pressure (P), tension (T), and null (B) axes, as well as nodal planes parameters (strike, dip and rake) from the deviatoric part of a given FMT. In our experimental configuration, P-axis plunge of a given AE source equal to 90° corresponds to the maximum compressive stress (σ_1) direction. T-axis plunge equal to 0° then aligns with the horizontal minimum compressive stress (σ_3) direction. To evaluate the variability in AE focal mechanisms, we calculated the 3D minimum rotation angle β ($0° \leq \beta \leq 120°$) between P and T axis directions of two focal mechanisms (Kagan, 2007). A low β suggests comparable focal mechanisms between two moment tensor solutions. For a specific subset of AE events, we also computed the mean 3D minimum rotation angles between all possible pairs of focal mechanisms included in the subset to assess their collective variability (e.g., Dresen et al., 2020; Goebel et al., 2017).

Following the shear-tensile source model (Vavryčuk, 2001), we additionally estimated the tensile angle α ($-90° \leq \alpha \leq 90°$), defined as the inclination angle between the slip vector and fault plane, using ISO and CLVD components (Vavryčuk, 2001, see equations 14, 15a therein). The value of $\alpha<0°$ corresponds to shear-enhanced compaction, $\alpha=0°$ represents pure shear (no volumetric change), and $\alpha>0°$ indicates shear-enhanced dilation.

Inversion of earthquake focal mechanisms to determine fault stress states is a well-established technique (e.g., Angelier, 1984; Hardebeck and Michael, 2006; Martínez-Garzón et al., 2014; Michael, 1987, 1984; Vavryčuk, 2014). The stress inversion algorithms assume that fault slip vectors are parallel to the resolved shear traction on the fault planes (Bott, 1959) (i.e., the Wallace-Bott hypothesis). The stress inversion requires FMTs that are dominantly DC sources. Previous studies (Busetti et al., 2014; Jia et al., 2018) suggest that the tensile angle of a DC-dominated source typically satisfies $|\alpha|<30°$; otherwise, the effect of tensile or compression component may not be ignored. In this study, we used well-constrained DC-dominated AE sources with $|\alpha|<30°$ for subsequent stress tensor inversion and focal plane analysis. To identify the more likely fault plane from two nodal planes provided by a

DC-dominated AE source, we can evaluate the susceptibility to shear failure for both nodal planes using the Mohr–Coulomb failure criterion (Vavryčuk, 2014), as expressed by

$$I = \frac{\widehat{\tau} - \mu(\widehat{\sigma} - 1)}{\mu + \sqrt{1 + \mu^2}} \quad (4)$$

where $\widehat{\tau}$ and $\widehat{\sigma}$ are the normalized shear and normal stresses and μ is the friction coefficient ($0.4 \leq \mu \leq 1.0$ was used). Fault instability I ranges from 0 to 1. Nodal planes with an orientation giving higher fault instability I correspond to likely slip planes (Martínez-Garzón et al., 2016; Vavryčuk, 2014). Fault planes with the higher instability I were used for stress tensor inversion in this study. We retrieved the stress field orientation from DC-dominated sources using an iterative inversion method (Vavryčuk, 2014) that best constrained the fault planes resulting in an improved accuracy of the resulting stress tensor.

4. Results

We reported experimental results from three experiments on one smooth (saw-cut) and two rough faults. Prior to fluid injection, samples were loaded close to critical stress states with similar values of σ_n' and τ among three experiments (Figs. 2a, 3a and Supplementary Fig. S7a). Subsequently, the six-stage fluid injection cycles resulted in fault slip and stress relaxation. Different fault slip patterns emerged, depending on fault surface roughness. In the following, we focus on injection-induced fault slip behavior and associated AE activity. The outcomes of rough fault #2 data analysis show that the obtained results are reproducible, which are presented in the Supplementary Materials.

4.1. Statistical characteristics of AE source mechanisms

The fluid injection cycles induced episodic slip events with different peak slip velocities observed on saw-cut and rough faults (Figs. 2a, 3a and Supplementary Fig. S7a). Average fault slip velocities correlated with AE rates for both smooth and rough fault. The spatial distribution of AE hypocenters varied visibly with fault surface roughness. For the smooth (saw-cut) fault, AE locations aligned tightly with the orientation of the pre-fabricated fault surface, forming a narrow band in a cross-section view with a half-width of 2 mm surrounding fault surface which was within the location accuracy (Fig. 4a and b). In contrast, for the rough faults we observed several localized clusters of AEs with broader fault-normal widths up to 10 mm, reflecting significant on- and off-fault damage (Fig. 4f, g and Supplementary Figs. S8a and b).

Using the combined criteria of NRMSD < 0.5 and MAXC < 0.05, we finally obtained high-quality AE source mechanisms of 3412, 2144 and 3398 events for the saw-cut fault, rough fault #1 and rough fault #2, respectively. The decomposed ISO, CLVD and DC components of FMT solutions are presented in Hudson plots (Hudson et al., 1989), color-coded by tensile angles (Figs. 4c, h and Supplementary Fig. S8c). Considering that FMTs with opposite signs of ISO and CLVD components are unphysical (Vavryčuk, 2001), we removed the FMTs with ISO>15% and CLVD <-15% or ISO <-15% and CLVD >15% (less than 7% of FMTs were removed) (Davidsen et al., 2021). In general, the source type of a shear-dominated AE event corresponds to a relatively high DC component (ISO and CLVD components are small). For both smooth and rough faults, most AE sources showed significant negative ISO and CLVD components representing compaction of pore space or crack closure (Figs. 4c, h and Supplementary Fig. S8c), also indicated by negative tensile angles. The mean tensile angles for all AE sources recorded in the smooth, rough fault #1 and rough fault #2 were about -17°, -19° and -12°, respectively (Supplementary Figs. S9c, S10c and S11c). A limited number of AEs (<14%) displayed source mechanisms with positive ISO and negative CLVD or vice versa. Compared to the smooth fault, grain-scale shear-enhanced dilation was more pronounced for rough faults. The mean DC percentage of all AE sources recorded in the smooth fault was ~52%, and reduced to ~41% and ~42% for the rough fault #1 and rough fault #2, respectively (Supplementary Figs. S9a, S10a and S11a). This observation suggests that failure mechanisms with significant non-DC components are favored by rough and complex fault geometry. Average non-DC components of AE sources accounted for up to 40% even for the saw-cut fault in our experiments, indicating the dominance of grain-scale cracking and frictional sliding accommodating shear-enhanced compaction. In contrast, displacement-driven stick-slip experiments on fine-grained granite saw-cut faults reported relatively smaller non-DC components of AE source mechanisms (Kwiatek et al., 2014b). This suggests that other factors (e.g., porosity, grain size and lithology) may also affect AE source mechanisms.

P-axis orientation of AEs for the smooth fault showed a high-density region with plunge angles ranging from 60° to 75° (Fig. 4d), and T-axis orientations formed a compact region with most plunge angles between 15° and 25°. In contrast, the variability of P-axis orientations increased significantly for the rough faults (Fig. 4i and Supplementary Fig. S8d), revealing fault roughness and associated off-fault damage zones which resulted in high variability in AE focal mechanisms. The increase in AE focal mechanism heterogeneity due to fault roughness was also characterized by a higher mean 3D rotation angle between all considered focal mechanisms, with values of ~68° and ~70° for the rough fault#1 and rough fault #2, respectively, in comparison to ~47° for the saw-cut fault (Supplementary Figs. S9d, S10d and S11d).

Using ternary diagrams (Frohlich, 1992), we classified faulting kinematics of calculated AE sources as normal faulting, strike-slip, reverse faulting, and hybrid mechanisms (mixed combination from two of these faulting regimes). In accordance with the imposed normal faulting regime, grain-scale fault slip events obtained from AE sources were dominated by normal faulting (Figs. 4e, j and Supplementary Fig. S8e), with a fraction up to about 50%, 39% and 33% for smooth fault, rough fault #1 and rough fault #2, respectively. In addition, substantial contributions of mixed normal and strike-slip faulting were observed.

4.2. Temporal evolution of AE sources associated with injection-induced fault slip

In response to fluid injection, slip along the smooth fault initiated with a delay that progressively decreased with subsequent injection cycles (Fig. 2a and Supplementary Table S1). During each fluid injection stage, the smooth fault displayed episodic slow stick-slip events with a peak slip velocity up to about 3.8 μm/s, accompanied by rapid stress drops and AE bursts (Fig. 2a). In contrast, for rough faults at similar loading conditions and fluid pressurization rates, induced slip events showed lower average slip velocities (~1.0 μm/s), with peak AE rates being slightly lower (Fig. 3a, Supplementary Fig. S7a and Supplementary Tables S2 and S3).

We used moving averages of AE-derived parameters in a time window containing 50 AE source mechanisms to capture their general temporal changes over the whole fault surface associated with injection-induced fault slip cycles. For the smooth fault, the percentage of ISO, P-axis plunge and tensile angle remained stationary during the time periods between consecutive slip events (Fig. 2b and c). The observed negative values of ISO, CLVD and tensile angle implied dominant shear-enhanced compaction. Approaching slip events, we observed an increase in the average DC components. The increase of DC components toward the onset of each slip event was accompanied by an appreciable rise in P-plunge, as well as reduction in focal mechanism variability (Fig. 2b–d). This suggests that local stresses homogenize at the onset of macroscopic slip events resulting in localized micro-shear sliding with enhanced contribution from DC components. Beyond slip onsets, rapid but small fluctuations in AE-derived parameters during ongoing slip reflected complex microscale failure/frictional processes possibly related to an evolving fault surface.

For rough faults, we also observed continuous shear-enhanced compaction, as expressed by negative DC and CLVD components and

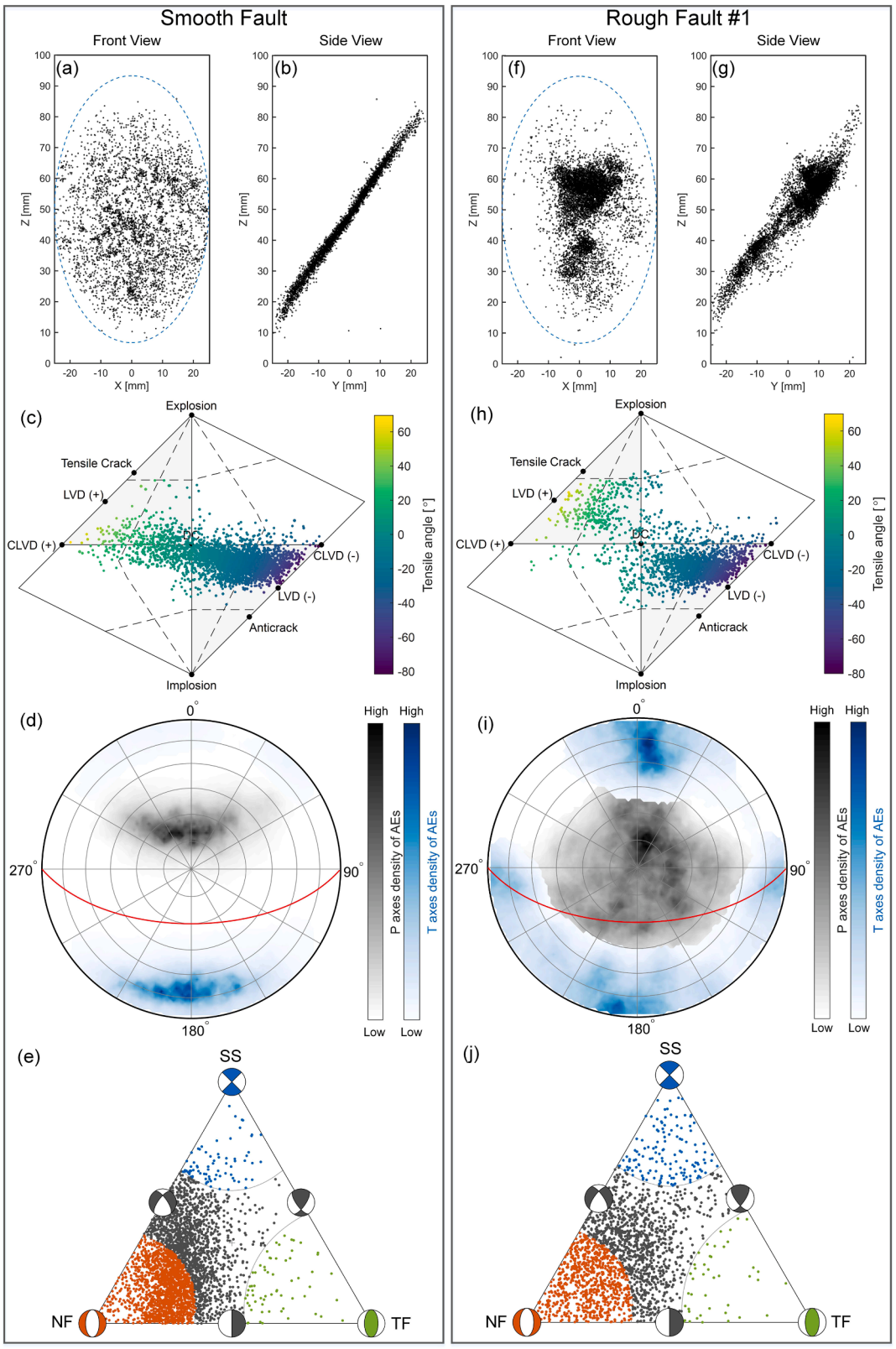

Fig. 4. (a and b) Front and cross-section views of AE hypocenters induced by fluid injection into the smooth (saw-cut) fault. The dashed blue curve shows boundary of the fault plane. (c) Hudson equal-area diagram (Hudson et al., 1989) presenting the source mechanisms of all AEs. The source mechanisms are color-coded by tensile angle, and the symbol sizes scale with AE magnitudes. DC: double couple; CLVD: compensated linear vector dipole; LVD: linear vector dipole. (d) P-axis and T-axis density maps calculated from FMT solutions of all AE sources (lower-hemisphere projection). Red curve depicts the projection of macroscopic pre-cut fault with a dip angle of 60°. (e) The ternary diagrams (Frohlich,1992) whose apices are the 'pure' mechanisms; NF: normal faulting; TF: thrust faulting; SS: strike-slip faulting. (f-j) Similar to (a-e) but for the rough fault #1.

negative tensile angles of AE source mechanisms (Fig. 3b, c and Supplementary Figs. S7b, c). However, there were no clear and consistent temporal changes of AE source characteristics. This included time-invariant DC percentages, as well as almost constant focal mechanism variability observable throughout entire fluid injection into the rough fault. This suggests that roughness and local stress heterogeneity prevail up to failure.

4.3. Fault plane parameters of AE sources and stress inversion

We assumed that a given FMT solution with the tensile angle satisfying $|\alpha| \leq 30^\circ$ was a DC-dominated AE source. Using this criterion, the number of well-constrained DC-dominant AE sources further reduced to 2514, 1238, and 2071 events, for the smooth, rough fault #1 and rough fault #2, respectively. For the smooth fault, we assumed that the more likely fault plane out of the two nodal planes for each AE focal mechanism was expected to be closer to the macroscopic fault plane orientation (i.e., selecting the nodal plane with the lower absolute value of dot product of the unit normal vectors between the AE nodal plane and macroscopic fault plane). For the rough faults, we selected the nodal plane with the higher instability coefficient I (see Eq. (4)) as the AE fault plane. The distributions of fault plane parameters (strike, dip and rake) are presented in Figs. 5a, 6a and Supplementary Fig. S12a for the smooth fault, rough fault #1 and rough fault #2, respectively.

The strike, dip and rake of the macroscopic pre-cut smooth fault plane are 90°, 60°, and −90°, respectively. As expected, the deformation along the smooth surface resulted in abundant AE sources with dominant DC mechanisms aligning well with the macroscopic fault plane orientation (Fig. 5a and d). AE focal mechanisms predominantly displayed the kinematics of normal and oblique normal faulting (Fig. 5a). Further, we statistically compared the orientation deviation between the microscopic AE fault plane and the macroscopic fault plane. The fault plane deflection ϑ, defined as the angle between an AE fault plane (more likely nodal plane) and the macroscopic fault plane using the dot product of their unit normal vectors $\mathbf{n}_{AE}$ and $\mathbf{n}_{fault}$ [i.e., $\vartheta = \arccos(|\mathbf{n}_{AE} \cdot \mathbf{n}_{fault}|)$], has a range from 0° to 90°. Most AE fault planes aligned well with the macroscopic fault plane (i.e., 80 % of AE fault plane orientations showed deviation angles < 20°, see Fig. 5b), and the fault plane deflection distribution had a peak value close to 10°.

For a given DC-dominated AE source, we calculated slip vector deflection θ between the AE unit slip vector $\mathbf{u}_{AE}$ and the macroscopic unit slip vector $\mathbf{u}_{fault}$ using their dot product, as defined by $\theta = \arccos(\mathbf{u}_{AE} \cdot \mathbf{u}_{fault})$. The range of θ is $0^\circ \leq \theta \leq 180^\circ$, with $\theta = 0^\circ$ and $\theta = 180^\circ$ corresponding to parallel slip vectors and parallel but opposite slip vectors $\mathbf{u}_{AE}$ and $\mathbf{u}_{fault}$, respectively. Slip vectors with deflection less than 44° accounted for 80 % of AE events (Fig. 5c), and the maximum of slip vectors showed a deflection of about 18°. Using the STRESSINVERSE code (Vavryčuk, 2014), the inverted stress orientation of σ_2 aligned with the far-field σ_2, but σ_1 and σ_3 directions were rotated by about 22° relative to applied far-field stress field (Fig. 5e).

The rough fault generally has non-planar fault topography and the resulting local AE fault patch orientation varies in space. For simplicity, for the rough faults the macroscopic pre-cut fault plane orientation was assumed to be the best-fitting planar surface inclined at 30° to the sample axis. This macroscopic fault orientation was used to compare with the local AE fault plane orientations. For the rough faults, the distribution of resolved strike, slip and rake of AE fault planes varied (Fig. 6a and Supplementary Fig. S12a). We observed a much broader range of AE fault plane orientations, and a small amount of AE rakes suggested local slip opposite to the macroscopic slip direction. In contrast to the smooth fault, the statistical analysis of fault plane deflection revealed a roughly bell-shaped distribution centered around 45°−55° (Fig. 6b and Supplementary Fig. S12b). The slip vector deflection angles frequently occurred in the range of 10°−80° (Fig. 6c and Supplementary Fig. S12c), much wider than observed for the smooth fault. Note that the inverted three principal stress orientations coincided with the applied far-field stress field (Fig. 6e).

4.4. On-fault and off-fault seismicity

The hierarchical structure of fault zones often reveals off-fault seismicity occurring in the surrounding of the principal slip surface (e.g. Page et al., 2011; Ross et al., 2017). In this section, we investigated the magnitude-frequency characteristics and source mechanisms of on-fault and off-fault AEs and their relation to fault geometry. The term 'on-fault AEs' referred to AE events with their hypocenters very close to the principal fault surface considering location uncertainties (i.e., fault-normal distance within 2 mm in this study), whereas we used the term 'off-fault AEs' to describe the remaining AE events that occurred outside of the principal slip surface. To calculate fault-normal distance, we first transformed all AE coordinates to the fault coordinate system (a Cartesian coordinate system on the macroscopic fault plane) and then estimated its normal distance relative to the scanned fault surface (Supplementary Fig. S13). We counted the number of AEs as a function of fault-normal distance within a bin width of 1 mm, and then calculated b-value and source mechanism-related parameters in each bin. To obtain reliable and accurate estimates of b-values, only AE catalogues in the spatial bin containing at least 120 AEs above M_c were considered. Considering that the well-constrained source mechanisms of AEs were lower than the total number of the catalogues, the spatial bin containing well-constrained AE sources higher than 50 was used to calculate the statistical characteristics of source mechanism-related parameters. The results are shown in Fig. 7 and Supplementary Fig. S14.

AE density showed a peak magnitude centered around the fault surface, and a rapid decay with distance toward the adjacent wall-rock (Fig. 7a, g and Supplementary Fig. S14a). The bell-shaped AE density distribution observed is in agreement with previous laboratory observations (Goebel et al., 2014) and reported in earthquakes for natural faults (Perrin et al., 2021; Powers and Jordan, 2010). These observations manifest the development of an off-fault damage zone and its spatial distribution of fracture density relative to the fault surface. Compared to the saw-cut fault, the initial rough faults showed wider damage zones (a factor of about 2), as indicated by a broader width of AE density distribution (Fig. 7a, g), in agreement with previous observations without fluid injection (Goebel et al., 2017). For the smooth fault, the b-value of AEs remained stable at a relatively low value of $b = 1.7 \pm 0.1$ around the fault surface and increased off-fault (Fig. 7b). The average DC component of AE source mechanisms on smooth fault had a peak value (58 %) in the proximity to the slip surface, and it gradually reduced to 40 % with increasing fault-normal distance (Fig. 7c). The observed changes were accompanied by an increase in focal mechanism variability toward off-fault (Fig. 7d). Further, the statistical results of fault plane deflection and slip vector deflection for on-fault AEs showed a low degree of deviation relative to the macroscopic fault plane, but their differences grew toward the wall-rock (Fig. 7e and f). Interestingly, the rough faults did not show a similar trend in the b-value and source mechanisms between on-fault and off-fault AEs (Fig. 7g–l and Supplementary Fig. S14), as observed in the smooth fault. In our experiments, the b-value of AEs for rough faults was found to be slightly lower than that of the saw-cut fault. This may be related to the fact that more AEs with larger magnitudes were localized around the high-stress regions for the rough faults (see Supplementary Figs. S3–S5 and Discussion section). Note that the overall AE catalogues do not have a frequency-magnitude distribution described by a single b-value above the magnitude of completeness (see Supplementary Figs. S3–S5 where one can see a much steeper decay for larger magnitudes). This might arise from the superposition of distributions with different b-values associated with different spatial regions since Supplementary Fig. S15 seems to be consistent with a single b-value for all considered AEs above M_c.

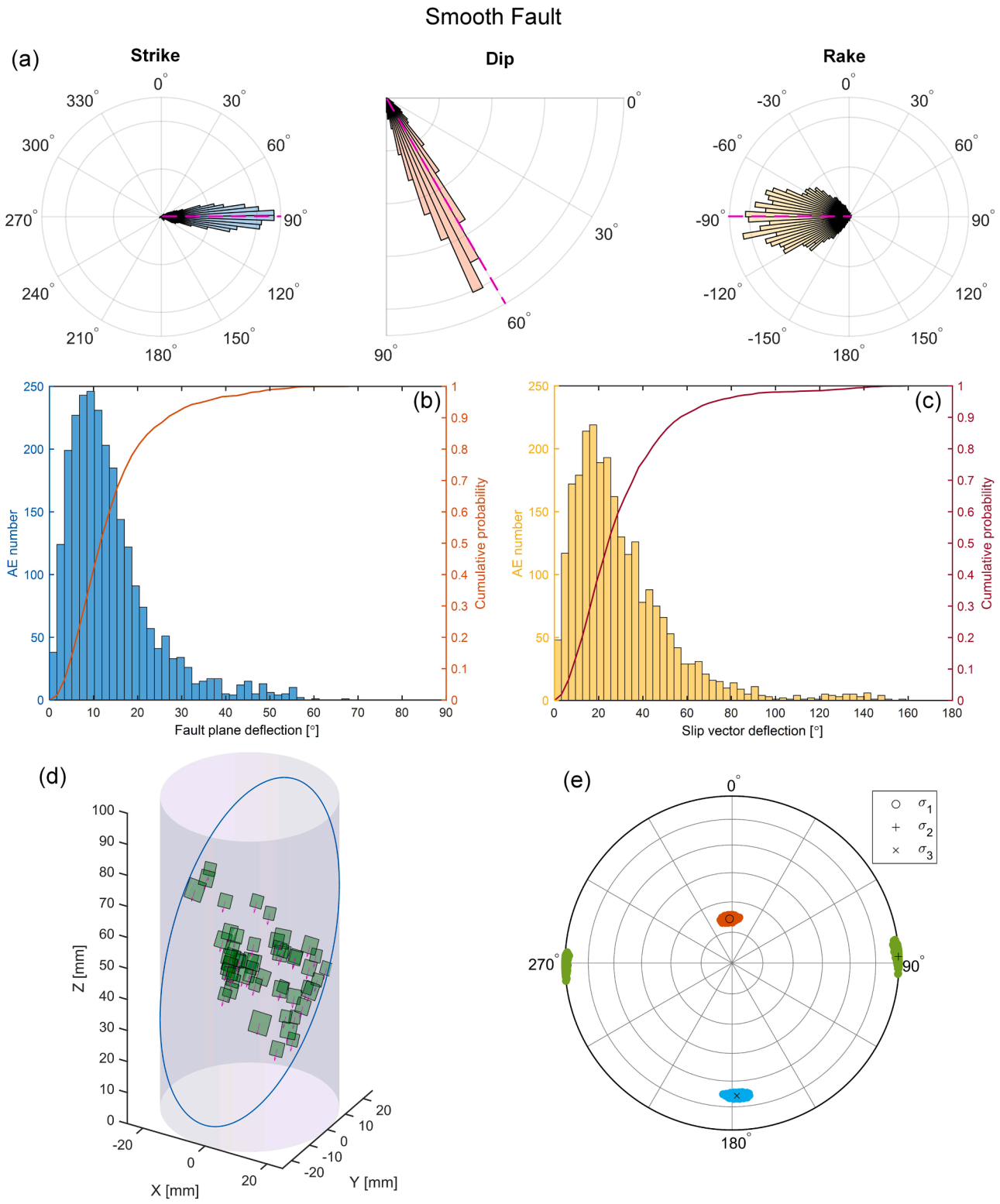

Fig. 5. (a) The polar histograms of nodal plane parameters (strike, dip and rake) of AEs for the smooth (saw-cut) fault. For reference, the strike, dip and rake of the macroscopic pre-cut fault plane are 90°, 60°, and −90°, respectively (dashed magenta lines). (b) Histogram of AE fault plane deflection distribution (left y-axis) and resulting cumulative probability (right y-axis). Fault plane deflection is defined as the angle between an AE fault plane and the macroscopic fault plane, which ranges from 0° to 90° (see main text for details). (c) Histogram of AE slip vector deflection distribution (left y-axis) and resulting cumulative probability (right y-axis). Slip vector deflection is calculated using dot product of unit slip vector of a given AE plane and the unit slip vector of macroscopic fault plane (see main text for details). (d) An example of spatial distribution of fault planes and slip vectors of some AE sources with hypocenters locating very close to the macroscopic fault plane. The inclined blue ellipse represents the external boundary of macroscopic pre-cut fault plane. Green rectangles represent fault plane orientations of AE sources with sizes proportional to AE magnitudes and magenta arrows indicate corresponding slip vectors. (e) Bootstrap derived density plot of principal stress orientations inverted from AE focal mechanisms dominated by double-couple events. The most likely orientations of principal stresses σ_1, σ_2, and σ_3 are marked with circle, addition and cross symbols, with corresponding azimuth/plunge of 356.8°/68.4°, 87.7°/0.3°, and 177.9°/21.6°, respectively.

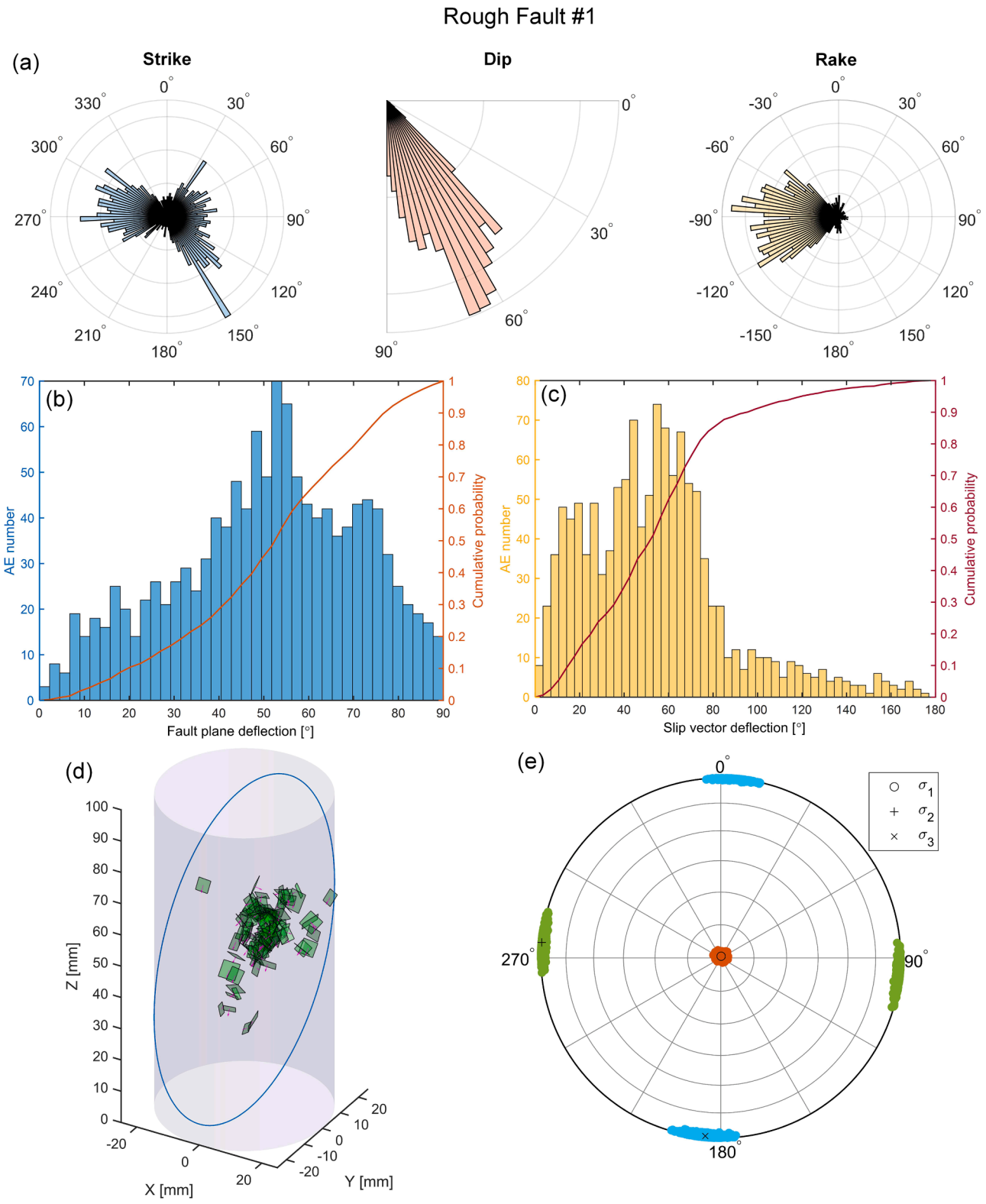

Fig. 6. (a) The polar histograms of nodal plane parameters (strike, dip and rake) of AEs for the rough fault #1. (b) Histogram of AE fault plane deflection distribution (left y-axis) and resulting cumulative probability (right y-axis). Fault plane deflection is defined as the angle between an AE fault plane and the macroscopic fault plane, which ranges from 0° to 90° (see main text for details). (c) Histogram of AE slip vector deflection distribution (left y-axis) and resulting cumulative probability (right y-axis). Slip vector deflection is calculated using dot product of unit slip vector of a given AE plane and the unit slip vector of macroscopic fault plane (see main text for details). (d) An example of spatial distribution of fault planes and slip vectors of some AE sources with hypocenters locating very close to the macroscopic fault plane. The inclined blue ellipse represents the external boundary of macroscopic pre-cut fault plane. Green rectangles represent fault plane orientations of AE sources with sizes proportional to AE magnitudes and magenta arrows indicate corresponding slip vectors. (e) Bootstrap derived density plot of principal stress orientations inverted from AE focal mechanisms dominated by double-couple events. The most likely orientations of principal stresses σ_1, σ_2, and σ_3 are marked with circle, addition and cross symbols, with corresponding azimuth/plunge of 10.9°/89.2°, 275.0°/0.1°, and 185.0°/0.8°, respectively.

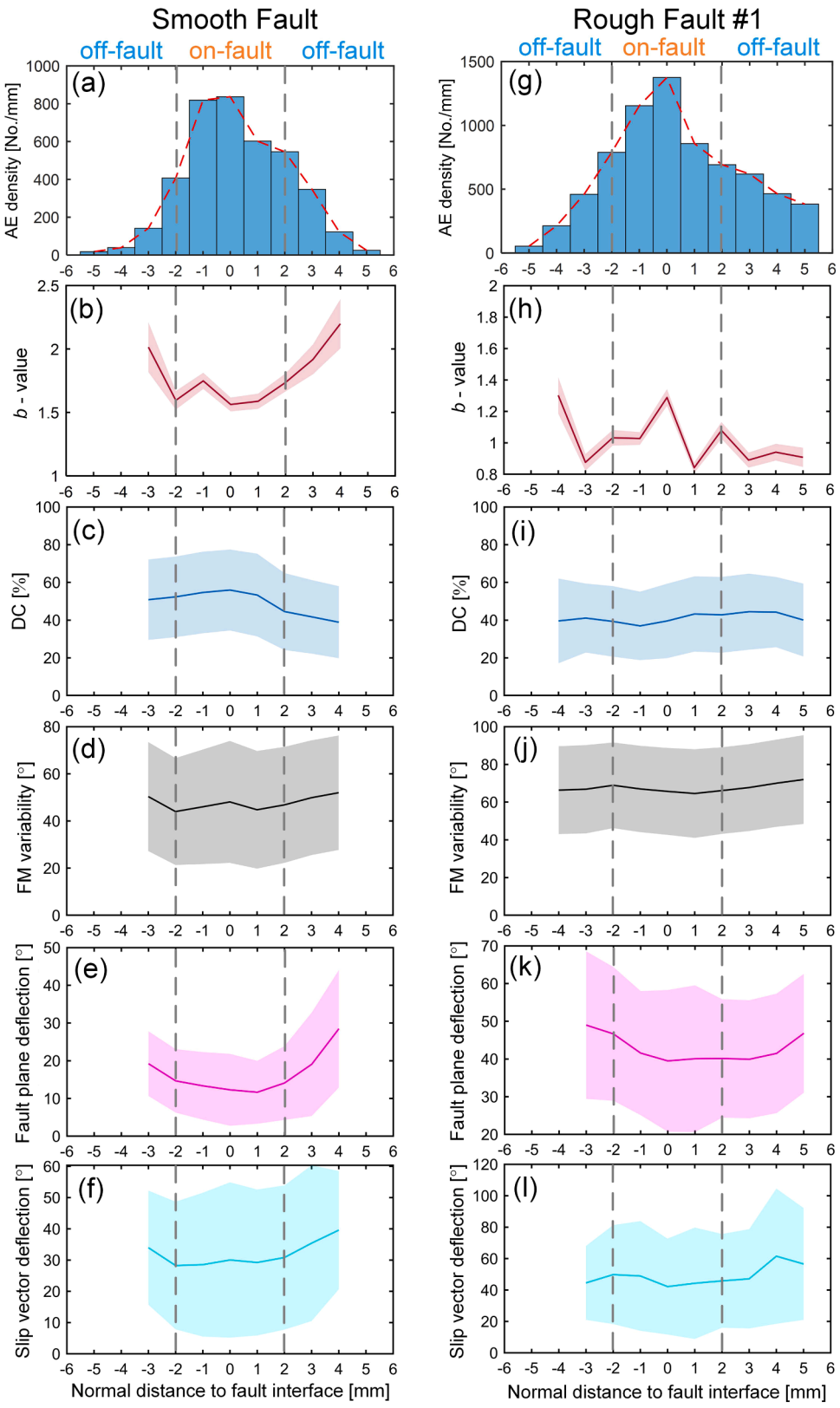

Fig. 7. (a–f) Distributions of AE event density, *b*-value, DC percentage, focal mechanism (FM) variability, fault plane deflection, and slip vector deflection as a function of normal distance from AE hypocenters to the smooth (saw-cut) fault interface, respectively. Positive fault-normal distance indicates AEs that are located within the hanging wall (upper rock block), and vice versa. We count the number of AEs as a function of normal distance from the scanned fault surface within a bin width of 1 mm, and then calculate *b*-value and source mechanism-related parameters in each bin. Uncertainties (standard deviations) of these parameters are indicated by the shaded areas. (g–l) Similar to (a–f), but for the rough fault #1.

5. Discussion

Natural faults exhibit complex geometries (Brodsky et al., 2016; Candela et al., 2012; Power et al., 1987; Power and Tullis, 1991; Renard et al., 2013), with their amplitude-to-wavelength ratios (roughness) typically ranging from 10^{-4} to 10^{-2}. Our saw-cut and fractured rough faults represent the two end-member cases, in which the fractured rough fault is more analogous to a new and less mature natural fault while the saw-cut fault may correspond to a mature, localized fault. The presence of fault roughness causes stress, strength and slip heterogeneity across the fault surface (Allam et al., 2019; Brodsky et al., 2016; Brown and Scholz, 1985; Chester and Chester, 2000; Dieterich and Smith, 2009) and further influences spatial distribution, magnitude, and source mechanisms of earthquakes (Cattania and Segall, 2021; Tal and Hager, 2018; Zielke et al., 2017).

We used an analytical model (Chester and Chester, 2000) to model the effect of fault geometry on the occurrence of local failure events and their spatial distribution. Assuming the homogeneous and linear-elastic half-space plane strain conditions and no opening at the interface, analytical solutions of the elastic stress distribution around a wavy frictional discontinuity in the upper half-space may be given by (Chester and Chester, 2000)

$$\sigma_{xx} = \sigma_{xx0} + Ale^{-lz}\left\{\frac{UEl}{4(1-\nu^2)}(-1+lz)\cos(lx) + \left[\sigma_{zz0}\left(1-k+2\mu^2\right) - \frac{\mu UEl}{4(1-\nu^2)}\right](-2+lz)\sin(lx)\right\} \tag{5a}$$

$$\sigma_{zz} = \sigma_{zz0} + Ale^{-lz}\left\{\frac{UEl}{4(1-\nu^2)}(-1-lz)\cos(lx) + \left[\sigma_{zz0}\left(1-k+2\mu^2\right) - \frac{\mu UEl}{4(1-\nu^2)}\right](-lz)\sin(lx)\right\} \tag{5b}$$

$$\sigma_{xz} = \sigma_{xz0} + Ale^{-lz}\left\{\frac{UEl}{4(1-\nu^2)}(-lz)\sin(lx) + \left[\sigma_{zz0}\left(1-k+2\mu^2\right) - \frac{\mu UEl}{4(1-\nu^2)}\right](-1+lz)\cos(lx)\right\} \tag{5c}$$

where σ_{xx0}, σ_{zz0}, and σ_{xz0} represent the background stress states (tensile stress is positive) with the coordinate directions x and z being parallel and perpendicular to the mean orientation of the surface, respectively; the wavy surface profile is described by $A\sin(lx)$ in which A is the amplitude and l is the wavenumber ($l = 2\pi/L$ with L being the wavelength); parameters of μ and k are determined by $\mu = -\sigma_{xz0}/\sigma_{zz0}$ and $k = \sigma_{xx0}/\sigma_{zz0}$, respectively; U represents the relative shear displacement (right-lateral); E and ν are Young's modulus and Poisson's ratio, respectively. In the present study, we simplified the measured saw-cut and rough fault profiles along slip direction as continuous sinusoidal (wavy) functions with different amplitudes and wavelengths in two dimensions (2D). We selected a representative fault profile along the fault slip direction (the major axis of the elliptical fault) to perform a static stress analysis at a given frictional shear displacement. For the saw-cut fault, one layer of cemented quartz grains in contact on the bare surface resulted in an undulated surface with small wavelengths (Fig. 8a). In contrast, the fractured rough fault profile displayed roughness with a large amplitude and wavelength that scaled with sample dimensions equivalent to the entire fault length (Fig. 9a). Prior to fluid injection, the far-field principal stresses applied in our tests were measured to be $\sigma_1 \approx 113$ MPa, $\sigma_3 \approx 35$ MPa and $\sigma_1 \approx 128$ MPa, $\sigma_3 \approx 35$ MPa (compression was positive here, contrary to the sign convention in Eq. 5) for saw-cut fault and rough fault #1, respectively, which could be converted to the local fault coordinate system (see Figs. 8a and 9a) with background stress tensor of σ_{xx0}, σ_{zz0}, and σ_{xz0}. We used the measured Young's modulus $E \approx 26$ GPa and Poisson's ratio $\nu \approx 0.17$ of the bulk material, as well as a given shear slip $U \approx 0.5$ mm for saw-cut fault and rough fault #1 to calculate the spatial distribution of static 2D stress tensor components of σ_{zz}, σ_{xx} and σ_{zx} around the fitted wavy interface in the upper half-space. The obtained stress tensor components were then rotated to calculate the local principal stresses σ_1 and σ_3 (compression was positive here for better readability), and we depicted the spatial variations in differential stress (σ_1-σ_3) and related them to the recorded AE hypocenters. Note that the presence of pore pressure has no effect on the differential stress distribution.

The numerical results show that for the saw-cut fault, differential stresses are high and localized in a narrow band with a half-width of 1–2 mm surrounding the fault surface (Fig. 8b). The analytical model here assumes static and pure elastic deformation in response to a given far-field stress state and frictional slip. Therefore, the gradual decrease of far-field stress σ_1 with injection-induced slip, and plastic deformation producing wear and damage are not accounted for in the model. However, the strong initial gradient in differential stress focusing on the principal slip surface agrees with localized grain comminution and asperity fracturing, causing abundant AE bursts along the saw-cut fault surface, as also observed in the post-mortem microstructures (Fig. 8c). Provided that b-value is inversely proportional to the differential stress level (Goebel et al., 2013; Scholz, 2015), the modelled high on-fault differential stresses are in good agreement with the observed low b-value for on-fault AEs (Fig. 7b).

In contrast, for the rough fault long-wavelength asperities result in persistent and large-scale stress heterogeneity and off-fault damage (Fig. 9). Spatially localized AE bursts correspond to regions of high differential stress. The high degree of stress heterogeneity around the rough surface may be responsible for the observed high variations in b-value with respect to fault-normal distance. Local stresses varying on the grain-scale also cause spatial variation of AE source kinematics. This is reflected in widely varying crack orientation, as confirmed by microstructure observations (Fig. 9c). This may explain why on- and off-fault AEs show similar source characteristics in rough faults (Fig. 7g–l). Our results highlight that injection-induced slips on juvenile and rough faults produce a high degree of focal mechanism heterogeneity. Such an observation has been reported from natural earthquakes (Bailey et al., 2010) and laboratory earthquakes driven by displacement-controlled loading (Dresen et al., 2020; Goebel et al., 2017). We attribute the increased focal mechanism variability for rough faults to a high degree of stress heterogeneity caused by complex fault geometry, and associated damage zones.

Whether fluid-induced seismicity and tectonic earthquakes share physical similarities remains debated. Previous studies have indicated that low-magnitude microseismic events ($M_w < 0$) associated with hydraulic fracturing might exhibit high b-values (often ~2) and non-double-couple source components (Atkinson et al., 2020; Schultz et al., 2020), which commonly has been explained as a result of activation of fracture networks in response to pore pressure changes. In contrast, injection-triggered sequences that include larger events ($M_w \geq 3$) typically have b-values of ~1 and dominant double-couple focal mechanisms (Atkinson et al., 2020; Schultz et al., 2020), similar to those observed for tectonic earthquakes. These large earthquakes are thought to occur due to reactivation of preexisting critically stressed faults outside the injection-perturbed zone and due to substantial release of tectonic stress. In our experiments, the boundary of simulated faults is

limited and fluid pressure is expected to perturb the whole fault cutting the rock sample. Thus, our recorded AE sources associated with fluid injection in the present study are more likely to mimic the microseismicity induced by fluid injection inside a field-scale reservoir. We documented appreciable non-DC components of AE source mechanisms for both smooth and rough faults during fluid injection, consistent with some fluid-induced microearthquakes reported from wellbore injection operations (Cuenot et al., 2006; Martínez-Garzón et al., 2017; Šílený et al., 2009). Fluid-induced seismicity from The Geysers geothermal reservoir in California revealed significant non-double-couple components (Martínez-Garzón et al., 2017), and their source mechanisms were magnitude dependent, with large-magnitude seismicity displaying more volumetric compaction (negative ISO). Likewise, a similar phenomenon was also observed in our experiments, particularly for rough faults (Supplementary Figs. S9e, S10e and S11e).

For the smooth fault, we found that the stress tensor inversion resulted in principal stresses σ_1 and σ_3 that were deviating by about 20° from the direction of far-field applied stresses (Fig. 5e). This is conceivable because most AEs are clustered around the principal slip zone. Thus, the stress orientations estimated from AE focal mechanisms reflect the local stress state surrounding the smooth on-fault region rather than the far-field stress state. The inverted principal stresses σ_1 and σ_3 oriented at about 50° and 40°, respectively, with respect to the fault plane suggest that the maximum shear stress directions within or close to the fault zone have been rotated toward the principal slip surface. Compared to the remotely applied stresses to host rocks, the rotation of regional stress within fractured fault zones has been attributed to the occurrence of shear faulting (or plastic flow) within fault zones causing local stress perturbations (Dresen, 1991; Hafner, 1951; Pollard and Segall, 1987) and/or to contrasting elastic properties

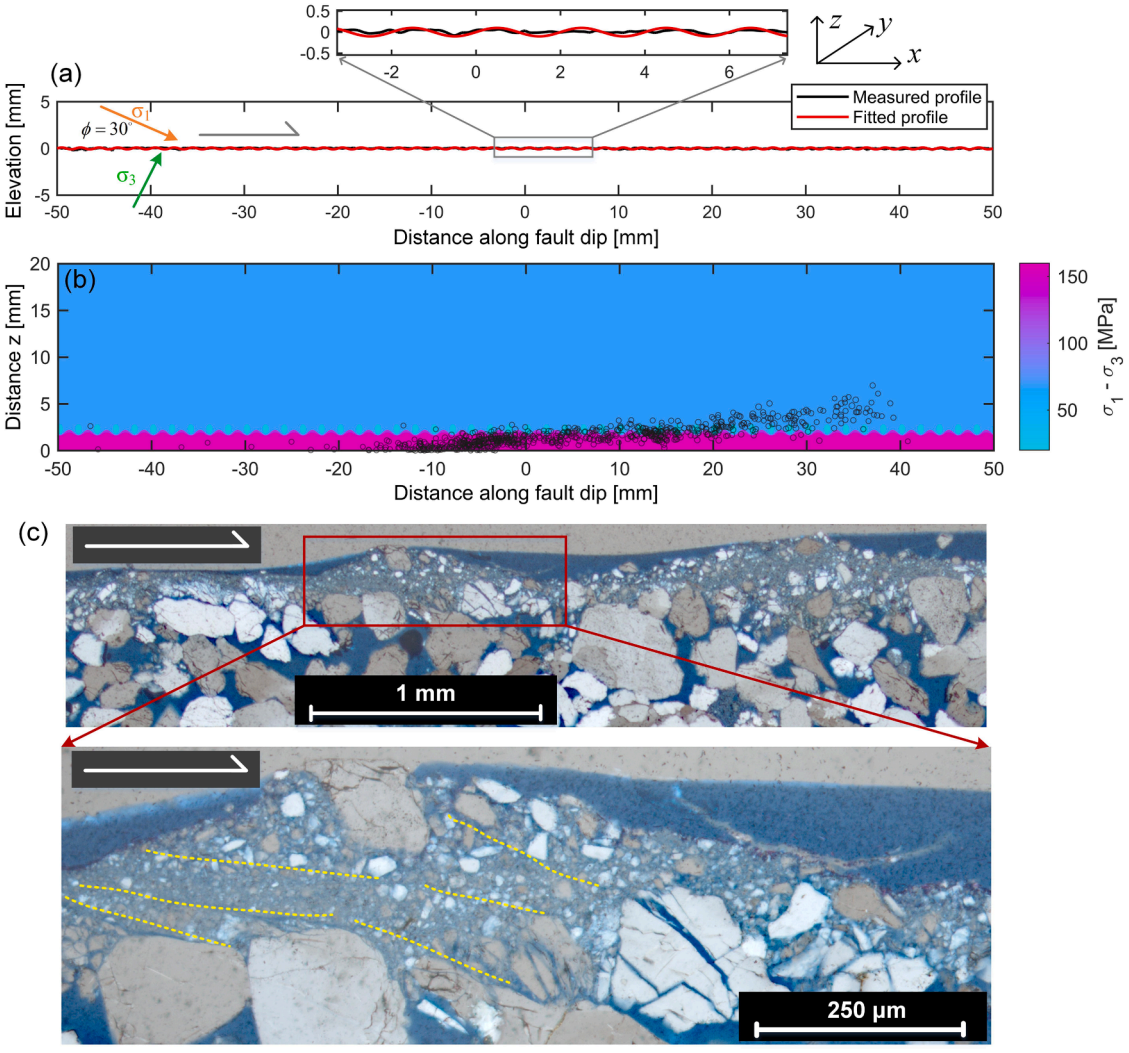

Fig. 8. (a) The measured profile (black curve) of saw-cut fault along fault up-dip direction (the major axis of the elliptical fault) and fitted profile (red curve) using a periodic sinusoidal function. The small-wavelength undulation arises from the contacts between adjacent quartz grains cemented on the fault surface. The far-field principal stresses $\sigma_1 \approx 113$ MPa and $\sigma_3 \approx 35$ MPa were applied to the interface prior to fluid injection with ϕ=30° between σ_1 and the fault surface (see Fig. 1a). The gray arrow shows slip direction of the lower rock block relative to its counterpart along fault up-dip. The local fault coordinate system (*x, y, z*) with *x* parallel to fault dip, *y* perpendicular to fault dip (out-of-plane), and *z* perpendicular to fault dip (in-plane) is also given for reference. (b) The spatial variation in local differential stress (σ_1-σ_3) and the distribution of experimentally recorded AEs (as indicated by open gray circles with sizes proportional to AE magnitudes) within the lower rock block during fluid injection. Because we map the distribution of (σ_1-σ_3) around the wavy interface profile along the major axis of the fault ellipse, here we only present the recorded AEs with hypocenters very close to it ($|y| < 5$ mm, see local fault coordinate system). (c) Fault-parallel cross-sectional microstructures of the smooth (saw-cut) fault using an optical microscopy, where red rectangle area is zoomed at the bottom panel. To prepare thin sections, the deformed rock sample was first impregnated with blue epoxy, and then carefully cut and polished parallel to slip direction and perpendicular to the fault plane. The white arrows indicate shear direction of the missing block. Grain fragmentation, shear-induced particle rotation and intense secondary fractures (Riedel R_1 shear fractures, indicated by dashed yellow lines) with a low angle with respect to principal slip surface are clearly observed.

between 'strong' host rocks and 'weak' fault zones (Casey, 1980; Faulkner et al., 2006; Rice, 1992). For the rough fault, however, AEs with high-variability focal mechanisms are spatially distributed inside and outside of the fault zone, and thus the inverted stress field based on all AE sources tends to collectively reflect the applied far-field stress conditions (Fig. 6e). Our observations suggest that even for relatively simple fault structures, stress tensor-inversion methods require caution in upscaling to far-field stress states.

Our study revealed that temporal changes of AE source mechanisms and micromechanics of deformation associated with fault slip during fluid injection were controlled by fault stress states. For the smooth fault, progressively increasing deformation approaching the onset of a large slip event was accompanied by an increasing DC percentage, and decreasing focal mechanism variability (Fig. 2). This indicates a gradual transition from distributed deformation to strain localization toward a principal slip surface. A gradual dominance of microscale shear failure approaching macroscopic faulting was also reported in brittle fracture tests of intact rock samples and stick-slip experiments on dry laboratory faults using AE monitoring (Dresen et al., 2020; Lockner et al., 1991) and in-situ dynamic X-ray imaging (Renard et al., 2019). However, no

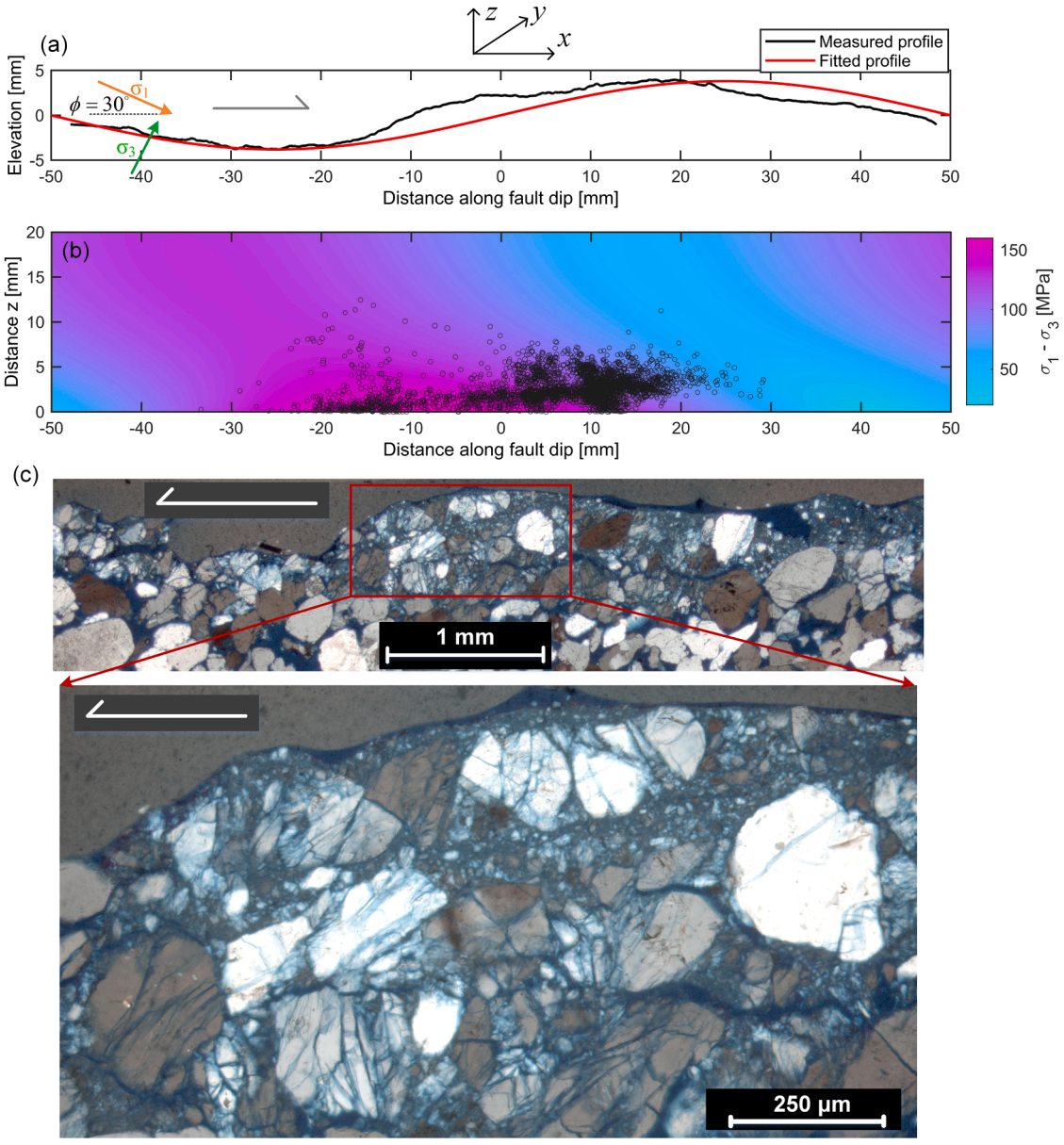

Fig. 9. (a) The measured profile (black curve) of the rough fault #1 along fault up-dip direction (the major axis of the elliptical fault) and fitted profile (red curve) using a periodic sinusoidal function. The far-field principal stresses $\sigma_1 \approx 128$ MPa and $\sigma_3 \approx 35$ MPa were applied to the interface prior to fluid injection with $\phi = 30^\circ$ between σ_1 and the fault surface (see Fig. 1a). The gray arrow shows slip direction of the lower rock block relative to its counterpart along fault up-dip. The local fault coordinate system (*x, y, z*) with *x* parallel to fault dip, *y* perpendicular to fault dip (out-of-plane), and *z* perpendicular to fault dip (in-plane) is also given for reference. (b) The spatial variation in local differential stress (σ_1-σ_3) and the distribution of experimentally recorded AEs (as indicated by open gray circles with sizes proportional to AE magnitudes) within the lower rock block during fluid injection. Because we map the distribution of (σ_1-σ_3) around the wavy interface profile along the major axis of the fault ellipse, here we only present the recorded AEs with hypocenters very close to it ($|y| < 5$ mm, see local fault coordinate system). (c) Fault-parallel cross-sectional microstructures of the rough fault #1 using an optical microscopy, where red rectangle area is zoomed at the bottom panel. To prepare thin sections, the deformed rock sample was first impregnated with blue epoxy, and then carefully cut and polished parallel to slip direction and perpendicular to the fault plane. The white arrows indicate shear direction of the missing block. Shear slip results in a thick off-fault damage zone surrounding the principal slip surface. Grain comminution and grain cracking with varying orientations reflect a high degree of local stress heterogeneity.

significant and consistent changes in AE focal mechanisms approaching large slips were found in rough faults. This is attributed to interactions between the dense fracture (damage) networks enhanced by a highly heterogeneous stress field, resulting in the distributed deformation outside of the fault surface (Fig. 9c). Also, field observations and numerical results both suggest that fracture interactions and highly transient local stress states may cause slip vectors to have variable orientations on a single fault surface (Cashman and Ellis, 1994; Pollard et al., 1993).

Fault plane orientations of DC-dominated AE sources characterize micro-failure planes on which local slip occurs. We found that for the smooth fault, the nodal plane orientations of AE sources did not exactly align with the pre-cut macroscopic fault plane, but rather had a dominant deviation angle at about 5°−20° (Fig. 5a and b). A number of geological surveys and laboratory experiments have documented the evolution of fault zone microstructures from distributed shearing to localized shearing along fault-parallel shear planes with increasing shear displacement (Logan, 2007; Logan et al., 1992). In our experiments, the two rock blocks with bare surfaces that came into contact only experienced a small amount of shear displacement (about 0.5 mm during fluid injection), and thus the resulting shear strain was low (assuming shear zone thickness ≈0.5–2 mm, see Figs. 8c, 9c). In the saw-cut fault, fault-parallel cross-sectional microstructure observations clearly show fine-grained gouge formation and development of an array of secondary fractures (i.e., Riedel R_1 shear structures) (Riedel, 1929) with small deviation angles of about 10°−20° (Fig. 8c), in agreement with previous studies on shear deformation within other gouge materials (Logan et al., 1992). For the rough fault, however, we observe a fault zone structure with a mixture of fine fault gouge and less-crushed grains with varying fracture orientations (Fig. 9c), presumably responsible for a high variation in local AE failure plane orientations and slip vectors (Fig. 6a–c).

Geological and geophysical measurements have indicated that fracture density within the damage zone decreases non-linearly (exponential or power-law decay) away from the fault core, coincident with the distribution of seismicity density with fault-normal distance (Faulkner et al., 2006; Perrin et al., 2021; Powers and Jordan, 2010). This is also confirmed by our decimeter-scale laboratory faults reactivated by fluid injection, independent of initial surface roughness. In contrast to natural fault topography or roughness that was commonly inferred from mapping the traces of surface ruptures (e.g., Okubo and Aki, 1987; Wesnousky, 1988) or from exhumed fault outcrops (e.g., Candela et al., 2012; Power et al., 1987; Power and Tullis, 1991; Renard et al., 2013), in our experiment we scanned fault surfaces in high spatial resolution and directly measured fault-normal distance between well-resolved AE hypocenters and the fault surface, allowing to distinguish and discuss properties of on-fault and off-fault seismicity. Our results show that for the relatively smooth fault, *b*-value of on-fault seismicity is lower than that of observed off-fault. At the same time, focal mechanisms of on-fault seismicity are less heterogeneous compared to off-fault seismicity. As fault roughness decreases with age and cumulative slip (Brodsky et al., 2011; Faulkner et al., 2011; Wesnousky, 1988), fault structural complexity is reflected by *b*-value and source mechanism changes along fault normal distance. AE clusters with low *b*-value and comparable source kinematics localized around the mature faults imply a local uniform high-stress field and relatively homogeneous material properties around the fault zone. A decreasing *b*-value trend toward a mature deformed fault zone has been also reported for natural earthquakes near southern California (Page et al., 2011; Ross et al., 2017).

6. Conclusions

We investigated the effect of fault roughness on source mechanisms of injection-induced seismicity using three fluid injection experiments associated with high-resolution AE monitoring. The laboratory faults with notably different surface roughness (smooth saw-cut versus fractured rough faults, respectively) were reactivated by progressive fluid overpressure, leading to episodic and slow fault slip. These episodic slips were associated with significant AE activity indicating local damage and stress evolution. We analyzed these processes using source characteristics of AEs including full moment tensor and stress tensor inversion, with main conclusions summarized below.

(1) The resolved AE full moment tensors highlight the significant non-DC contributions, especially for rough faults, but injection-induced slips on rough faults produce a high degree of focal mechanism heterogeneity.
(2) For the smooth fault, the inverted stress field from focal mechanisms of localized AEs close to the fault zone deviates from the far-field applied stress field, likely due to the occurrence of shear faulting within fault zones and/or to contrasting elastic properties between 'strong' host rocks and 'weak' fault zones.
(3) The observed inconsistency between nodal planes of AE sources and macroscopic fault plane orientation is attributed to the development of secondary fracture networks as found in the microstructures surrounding the fault surface.
(4) For the smooth fault, we observed progressively increasing DC components of AE sources and decreasing focal mechanism variability when approaching the onset of induced slip events, indicating a gradual transition from distributed deformation to shear localization toward the principal slip surface. However, this trend was not clearly seen on rough faults due to complex fault zone structures.
(5) For relatively smooth and mature faults, the *b*-value of on-fault AEs is lower and their focal mechanisms are less heterogeneous, compared to off-fault AEs.

CRediT authorship contribution statement

Lei Wang: Writing – original draft, Methodology, Investigation, Formal analysis, Data curation, Conceptualization. **Grzegorz Kwiatek:** Writing – review & editing, Software, Methodology. **Marco Bohnhoff:** Writing – review & editing, Resources, Funding acquisition. **Erik Rybacki:** Writing – review & editing, Visualization. **Georg Dresen:** Writing – review & editing, Supervision, Investigation, Funding acquisition.

Declaration of Competing Interest

The authors declare that they have no known competing financial interests or personal relationships that could have appeared to influence the work reported in this paper.

Data availability

Data will be made available on request.

Acknowledgments

The authors are grateful to Stefan Gehrmann for assistance with sample preparation and thin-sections, and to Michael Naumann for experimental guidance. The authors appreciate much help provided by Valerian Schuster for thin-section microscopy observations. We thank Ryan Schultz, an anonymous reviewer and the Editor for providing constructive comments that have substantially improved the present study. L.W. acknowledges in-house postdoc funding provided by GFZ-Potsdam. G.D. acknowledges funding from BMBF project STIMTEC-X 03G0901C.

Supplementary materials

Supplementary material associated with this article can be found, in the online version, at doi:10.1016/j.epsl.2023.118515.

References

Allam, A.A., Kroll, K.A., Milliner, C.W.D., Richards-Dinger, K.B., 2019. Effects of fault roughness on coseismic slip and earthquake locations. J. Geophys. Res. Solid Earth 124, 11336–11349. https://doi.org/10.1029/2018JB016216.

Angelier, J., 1984. Tectonic analysis of fault slip data sets. J. Geophys. Res. 89 https://doi.org/10.1029/JB089iB07p05835.

Atkinson, G.M., Eaton, D.W., Igonin, N., 2020. Developments in understanding seismicity triggered by hydraulic fracturing. Nat. Rev. Earth Environ. 1, 264–277. https://doi.org/10.1038/s43017-020-0049-7.

Bailey, I.W., Ben-Zion, Y., Becker, T.W., Holschneider, M., 2010. Quantifying focal mechanism heterogeneity for fault zones in central and southern California. Geophys. J. Int. 183 https://doi.org/10.1111/j.1365-246X.2010.04745.x.

Blanke, A., Kwiatek, G., Goebel, T.H.W., Bohnhoff, M., Dresen, G., 2020. Stress drop–magnitude dependence of acoustic emissions during laboratory stick-slip. Geophys. J. Int. 224, 1371–1380. https://doi.org/10.1093/gji/ggaa524.

Bott, M.H.P., 1959. The mechanics of oblique slip faulting. Geol. Mag. 96 https://doi.org/10.1017/S0016756800059987.

Brodsky, E.E., Gilchrist, J.J., Sagy, A., Collettini, C., 2011. Faults smooth gradually as a function of slip. Earth Planet. Sci. Lett. 302, 185–193. https://doi.org/10.1016/J.EPSL.2010.12.010.

Brodsky, E.E., Kirkpatrick, J.D., Candela, T., 2016. Constraints from fault roughness on the scale-dependent strength of rocks. Geology 44, 19–22. https://doi.org/10.1130/G37206.1.

Brown, S.R., Scholz, C.H., 1985. Closure of random elastic surfaces in contact. J. Geophys. Res. Solid Earth 90, 5531–5545. https://doi.org/10.1029/JB090iB07p05531.

Busetti, S., Jiao, W., Reches, Z., 2014. Geomechanics of hydraulic fracturing microseismicity: part 1. Shear, hybrid, and tensile events. Am. Assoc. Pet. Geol. Bull. 98 https://doi.org/10.1306/05141413123.

Candela, T., Renard, F., Klinger, Y., Mair, K., Schmittbuhl, J., Brodsky, E.E., 2012. Roughness of fault surfaces over nine decades of length scales. J. Geophys. Res. Solid Earth 117, B08409. https://doi.org/10.1029/2011JB009041.

Casey, M., 1980. Mechanics of shear zones in isotropic dilatant materials. J. Struct. Geol. 2, 143–147. https://doi.org/10.1016/0191-8141(80)90044-9.

Cashman, P.H., Ellis, M.A., 1994. Fault interaction may generate multiple slip vectors on a single fault surface. Geology 22, 1123–1126.

Cattania, C., Segall, P., 2021. Precursory slow slip and foreshocks on rough faults. J. Geophys. Res. Solid Earth 126. https://doi.org/10.1029/2020JB020430 e2020JB020430.

Chester, F.M., Chester, J.S., 2000. Stress and deformation along wavy frictional faults. J. Geophys. Res. Solid Earth 105, 23421–23430. https://doi.org/10.1029/2000JB900241.

Cuenot, N., Charléty, J., Dorbath, L., Haessler, H., 2006. Faulting mechanisms and stress regime at the European HDR site of Soultz-sous-Forêts, France. Geothermics 35, 561–575. https://doi.org/10.1016/j.geothermics.2006.11.007.

Davidsen, J., Goebel, T., Kwiatek, G., Stanchits, S., Baró, J., Dresen, G., 2021. What controls the presence and characteristics of aftershocks in rock fracture in the lab? J. Geophys. Res. Solid Earth 126. https://doi.org/10.1029/2021JB022539 e2021JB022539.

Dieterich, J.H., Smith, D.E., 2009. Nonplanar faults: mechanics of slip and off-fault damage. Pure Appl. Geophys. 166, 1799–1815. https://doi.org/10.1007/s00024-009-0517-y.

Dresen, G., 1991. Stress distribution and the orientation of Riedel shears. Tectonophysics 188, 239–247. https://doi.org/10.1016/0040-1951(91)90458-5.

Dresen, G., Kwiatek, G., Goebel, T., Ben-Zion, Y., 2020. Seismic and aseismic preparatory processes before large stick–slip failure. Pure Appl. Geophys. 177, 5741–5760. https://doi.org/10.1007/s00024-020-02605-x.

Ellsworth, W.L., 2013. Injection-induced earthquakes. Science (80-.) 341, 1225942. https://doi.org/10.1126/science.1225942.

Fang, Z., Dunham, E.M., 2013. Additional shear resistance from fault roughness and stress levels on geometrically complex faults. J. Geophys. Res. Solid Earth 118, 3642–3654. https://doi.org/10.1002/jgrb.50262.

Faulkner, D.R., Mitchell, T.M., Healy, D., Heap, M.J., 2006. Slip on "weak" faults by the rotation of regional stress in the fracture damage zone. Nature 444, 922–925.

Faulkner, D.R., Mitchell, T.M., Jensen, E., Cembrano, J., 2011. Scaling of fault damage zones with displacement and the implications for fault growth processes. J. Geophys. Res. Solid Earth 116. https://doi.org/10.1029/2010JB007788.

Fehler, M.C., 1989. Stress control of seismicity patterns observed during hydraulic fracturing experiments at the Fenton Hill hot dry rock geothermal energy site, New Mexico. Int. J. Rock Mech. Min. Sci. 26 https://doi.org/10.1016/0148-9062(89)91971-2.

Frohlich, C., 1994. Earthquakes with non-double-couple mechanisms. Science (80-.) 264. https://doi.org/10.1126/science.264.5160.804.

Frohlich, C., 1992. Triangle diagrams: ternary graphs to display similarity and diversity of earthquake focal mechanisms. Phys. Earth Planet. Inter. 75, 193–198. https://doi.org/10.1016/0031-9201(92)90130-N.

Goebel, T.H., Schorlemmer, D., Becker, T.W., Dresen, G., Sammis, C.G., 2013. Acoustic emissions document stress changes over many seismic cycles in stick-slip experiments. Geophys. Res. Lett. 40, 2049–2054.

Goebel, T.H.W., Becker, T.W., Sammis, C.G., Dresen, G., Schorlemmer, D., 2014. Off-fault damage and acoustic emission distributions during the evolution of structurally complex faults over series of stick-slip events. Geophys. J. Int. 197, 1705–1718. https://doi.org/10.1093/gji/ggu074.

Goebel, T.H.W., Kwiatek, G., Becker, T.W., Brodsky, E.E., Dresen, G., 2017. What allows seismic events to grow big?: Insights from b-value and fault roughness analysis in laboratory stick-slip experiments. Geology 45, 815–818. https://doi.org/10.1130/G39147.1.

Graham, C.C., Stanchits, S., Main, I.G., Dresen, G., 2010. Comparison of polarity and moment tensor inversion methods for source analysis of acoustic emission data. Int. J. Rock Mech. Min. Sci. 47, 161–169. https://doi.org/10.1016/j.ijrmms.2009.05.002.

Guérin-Marthe, S., Kwiatek, G., Wang, L., Bonnelye, A., Martínez-Garzón, P., Dresen, G., 2023. Preparatory slip in laboratory faults: effects of roughness and load point velocity. J. Geophys. Res. Solid Earth 128. https://doi.org/10.1029/2022JB025511 e2022JB025511.

Guglielmi, Y., Cappa, F., Avouac, J.-P., Henry, P., Elsworth, D., 2015. Seismicity triggered by fluid injection–induced aseismic slip. Science (80-.) 348, 1224–1226. https://doi.org/10.1126/science.aab0476.

Hafner, W., 1951. Stress distribution and faulting. Geol. Soc. Am. Bull. 62, 373–398. https://doi.org/10.1130/0016-7606(1951)62[373:SDAF]2.0.CO;2.

Hardebeck, J.L., Michael, A.J., 2006. Damped regional-scale stress inversions: methodology and examples for southern California and the Coalinga aftershock sequence. J. Geophys. Res. Solid Earth 111. https://doi.org/10.1029/2005JB004144.

Holmgren, J.M., Kwiatek, G., Werner, M.J., 2023. Nonsystematic rupture directivity of geothermal energy induced microseismicity in Helsinki, Finland. J. Geophys. Res. Solid Earth 128. https://doi.org/10.1029/2022JB025226.

Horálek, J., Jechumtálová, Z., Dorbath, L., Šílený, J., 2010. Source mechanisms of micro-earthquakes induced in a fluid injection experiment at the HDR site Soultz-sous-Forêts (Alsace) in 2003 and their temporal and spatial variations. Geophys. J. Int. 181, 1547–1565. https://doi.org/10.1111/j.1365-246X.2010.04506.x.

Hudson, J.A., Pearce, R.G., Rogers, R.M., 1989. Source type plot for inversion of the moment tensor. J. Geophys. Res. Solid Earth 94, 765–774. https://doi.org/10.1029/JB094iB01p00765.

Jia, S.Q., Eaton, D.W., Wong, R.C.K., 2018. Stress inversion of shear-tensile focal mechanisms with application to hydraulic fracture monitoring. Geophys. J. Int. 215 https://doi.org/10.1093/gji/ggy290.

Julian, B.R., Miller, A.D., Foulger, G.R., 1998. Non-double-couple earthquakes 1. Theory. Rev. Geophys. 36, 525–549. https://doi.org/10.1029/98RG00716.

Kagan, Y.Y., 2007. Simplified algorithms for calculating double-couple rotation. Geophys. J. Int. 171, 411–418. https://doi.org/10.1111/J.1365-246X.2007.03538.X/3/M_171-1-411-EQ042.JPEG.

Knopoff, L., Randall, M.J., 1970. The compensated linear-vector dipole: a possible mechanism for deep earthquakes. J. Geophys. Res. 75, 4957–4963. https://doi.org/10.1029/JB075I026P04957.

Kwiatek, G., Charalampidou, E.-M., Dresen, G., Stanchits, S., 2014a. An improved method for seismic moment tensor inversion of acoustic emissions through assessment of sensor coupling and sensitivity to incidence angle. Int. J. Rock Mech. Min. Sci. 65, 153–161. https://doi.org/10.1016/j.ijrmms.2013.11.005.

Kwiatek, G., Goebel, T.H.W., Dresen, G., 2014b. Seismic moment tensor and b value variations over successive seismic cycles in laboratory stick-slip experiments. Geophys. Res. Lett. 41, 5838–5846. https://doi.org/10.1002/2014GL060159.

Kwiatek, G., Martínez-Garzón, P., Bohnhoff, M., 2016. HybridMT: a MATLAB/Shell environment package for seismic moment tensor inversion and refinement. Seismol. Res. Lett. 87, 964–976.

Lockner, D.A., Byerlee, J.D., Kuksenko, V., Ponomarev, A., Sidorin, A., 1991. Quasi-static fault growth and shear fracture energy in granite. Nature 350, 39–42. https://doi.org/10.1038/350039a0.

Logan, J.M., 2007. The progression from damage to localization of displacement observed in laboratory testing of porous rocks. Geol. Soc. Spec. Publ. 289, 75–87. https://doi.org/10.1144/SP289.5.

Logan, J.M., Dengo, C.A., Higgs, N.G., Wang, Z.Z., 1992. Fabrics of experimental fault zones: their development and relationship to mechanical behavior. Int. Geophys. 51, 33–67. https://doi.org/10.1016/S0074-6142(08)62814-4.

Martínez-Garzón, P., Kwiatek, G., Bohnhoff, M., Dresen, G., 2017. Volumetric components in the earthquake source related to fluid injection and stress state. Geophys. Res. Lett. 44, 800–809. https://doi.org/10.1002/2016GL071963.

Martínez-Garzón, P., Kwiatek, G., Bohnhoff, M., Dresen, G., 2016. Impact of fluid injection on fracture reactivation at The Geysers geothermal field. J. Geophys. Res. Solid Earth 121. https://doi.org/10.1002/2016JB013137.

Martínez-Garzón, P., Kwiatek, G., Ickrath, M., Bohnhoff, M., 2014. MSATSI: a MATLAB package for stress inversion combining solid classic methodology, a new simplified user-handling, and a visualization tool. Seismol. Res. Lett. 85 https://doi.org/10.1785/0220130189.

McLaskey, G.C., Lockner, D.A., 2014. Preslip and cascade processes initiating laboratory stick slip. J. Geophys. Res. Solid Earth 119, 6323–6336. https://doi.org/10.1002/2014JB011220.

Michael, A.J., 1987. Use of focal mechanisms to determine stress: a control study. J. Geophys. Res. 92 https://doi.org/10.1029/JB092iB01p00357.

Michael, A.J., 1984. Determination of stress from slip data: faults and folds. J. Geophys. Res. Solid Earth 89, 11517–11526. https://doi.org/10.1029/JB089iB13p11517.

Miller, A.D., Foulger, G.R., Julian, B.R., 1998. Non-double-couple earthquakes 2. Observations. Rev. Geophys. 36 https://doi.org/10.1029/98RG00717.
Moeck, I., Kwiatek, G., Zimmermann, G., 2009. Slip tendency analysis, fault reactivation potential and induced seismicity in a deep geothermal reservoir. J. Struct. Geol. 31 https://doi.org/10.1016/j.jsg.2009.06.012.
Okubo, P.G., Aki, K., 1987. Fractal geometry in the San Andreas fault system. J. Geophys. Res. Solid Earth 92, 345–355. https://doi.org/10.1029/JB092IB01P00345.
Page, M.T., Alderson, D., Doyle, J., 2011. The magnitude distribution of earthquakes near Southern California faults. J. Geophys. Res. Solid Earth 116, 12309. https://doi.org/10.1029/2010JB007933.
Perrin, C., Waldhauser, F., Scholz, C.H., 2021. The shear deformation zone and the smoothing of faults with displacement. J. Geophys. Res. Solid Earth 126. https://doi.org/10.1029/2020JB020447 e2020JB020447.
Pollard, D.D., Saltzer, S.D., Rubin, A.M., 1993. Stress inversion methods: are they based on faulty assumptions? J. Struct. Geol. 15 https://doi.org/10.1016/0191-8141(93)90176-B.
Pollard, D.D., Segall, P., 1987. Theoretical displacements and stresses near fractures in rock: with applications to faults, joints, veins, dikes, and solution surfaces. Fract. Mech. Rock 277–349. https://doi.org/10.1016/b978-0-12-066266-1.50013-2.
Power, W.L., Tullis, T.E., 1991. Euclidean and fractal models for the description of rock surface roughness. J. Geophys. Res. Solid Earth 96, 415–424. https://doi.org/10.1029/90JB02107.
Power, W.L., Tullis, T.E., Brown, S.R., Boitnott, G.N., Scholz, C.H., 1987. Roughness of natural fault surfaces. Geophys. Res. Lett. 14, 29–32. https://doi.org/10.1029/GL014I001P00029.
Powers, P.M., Jordan, T.H., 2010. Distribution of seismicity across strike-slip faults in California. J. Geophys. Res. Solid Earth 115, 5305. https://doi.org/10.1029/2008JB006234.
Renard, F., Candela, T., Bouchaud, E., 2013. Constant dimensionality of fault roughness from the scale of micro-fractures to the scale of continents. Geophys. Res. Lett. 40, 83–87. https://doi.org/10.1029/2012GL054143.
Renard, F., McBeck, J., Kandula, N., Cordonnier, B., Meakin, P., Ben-Zion, Y., 2019. Volumetric and shear processes in crystalline rock approaching faulting. Proc. Natl. Acad. Sci. U. S. A. 116, 16234–16239. https://doi.org/10.1073/pnas.1902994116.
Rice, J.R., 1992. Fault stress states, pore pressure distributions, and the weakness of the San Andreas fault. Int. Geophys. 51, 475–503. https://doi.org/10.1016/S0074-6142(08)62835-1.
Riedel, W., 1929. Zur Mechanik Geologischer Brucherscheinungen. Zentral-blatt fur Mineralogie. Geol. und Paleontol. B 354–368.
Ross, Z.E., Hauksson, E., Ben-Zion, Y., 2017. Abundant off-fault seismicity and orthogonal structures in the San Jacinto fault zone. Sci. Adv. 3 https://doi.org/10.1126/SCIADV.1601946/SUPPL_FILE/1601946_SM.PDF.
Scholz, C.H., 2015. On the stress dependence of the earthquake b value. Geophys. Res. Lett. 42, 1399–1402. https://doi.org/10.1002/2014GL062863.
Schultz, R., Skoumal, R.J., Brudzinski, M.R., Eaton, D., Baptie, B., Ellsworth, W., 2020. Hydraulic fracturing-induced seismicity. Rev. Geophys. 58 https://doi.org/10.1029/2019RG000695 e2019RG000695.
Sellers, E.J., Kataka, M.O., Linzer, L.M., 2003. Source parameters of acoustic emission events and scaling with mining-induced seismicity. J. Geophys. Res. Solid Earth 108. https://doi.org/10.1029/2001jb000670.
Shi, Y., Bolt, B.A., 1982. The standard error of the magnitude-frequency b value. Bull. Seismol. Soc. Am. 72, 1677–1687. https://doi.org/10.1785/BSSA0720051677.
Šílený, J., Hill, D.P., Eisner, L., Cornet, F.H., 2009. Non–double-couple mechanisms of microearthquakes induced by hydraulic fracturing. J. Geophys. Res. Solid Earth 114. https://doi.org/10.1029/2008JB005987.
Stierle, E., Vavryčuk, V., Kwiatek, G., Charalampidou, E.-M., Bohnhoff, M., 2016. Seismic moment tensors of acoustic emissions recorded during laboratory rock deformation experiments: sensitivity to attenuation and anisotropy. Geophys. J. Int. 205, 38–50. https://doi.org/10.1093/gji/ggw009.
Tal, Y., Hager, B.H., 2018. The slip behavior and source parameters for spontaneous slip events on rough faults subjected to slow tectonic loading. J. Geophys. Res. Solid Earth 123, 1810–1823. https://doi.org/10.1002/2017JB014737.
Thompson, B.D., Young, R.P., Lockner, D.A., 2009. Premonitory acoustic emissions and stick-slip in natural and smooth-faulted Westerly granite. J. Geophys. Res. Solid Earth 114. https://doi.org/10.1029/2008JB005753.
Thompson, B.D., Young, R.P., Lockner, D.A., 2005. Observations of premonitory acoustic emission and slip nucleation during a stick slip experiment in smooth faulted Westerly granite. Geophys. Res. Lett. 32 https://doi.org/10.1029/2005GL022750.
Vavryčuk, V., 2014. Iterative joint inversion for stress and fault orientations from focal mechanisms. Geophys. J. Int. 199, 69–77. https://doi.org/10.1093/gji/ggu224.
Vavryčuk, V., 2001. Inversion for parameters of tensile earthquakes. J. Geophys. Res. Solid Earth 106, 16339–16355. https://doi.org/10.1029/2001JB000372.
Wang, L., Dresen, G., Rybacki, E., Bonnelye, A., Bohnhoff, M., 2020a. Pressure-dependent bulk compressibility of a porous granular material modeled by improved contact mechanics and micromechanical approaches: effects of surface roughness of grains. Acta Mater 188, 259–272. https://doi.org/10.1016/j.actamat.2020.01.063.
Wang, L., Kwiatek, G., Rybacki, E., Bohnhoff, M., Dresen, G., 2020b. Injection-induced seismic moment release and laboratory fault slip: implications for fluid-induced seismicity. Geophys. Res. Lett. 47 https://doi.org/10.1029/2020GL089576 e2020GL089576.
Wang, L., Kwiatek, G., Rybacki, E., Bonnelye, A., Bohnhoff, M., Dresen, G., 2020c. Laboratory study on fluid-induced fault slip behavior: the role of fluid pressurization rate. Geophys. Res. Lett. 47 https://doi.org/10.1029/2019GL086627 e2019GL086627.
Wang, L., Rybacki, E., Bonnelye, A., Bohnhoff, M., Dresen, G., 2021. Experimental investigation on static and dynamic bulk moduli of dry and fluid-saturated porous sandstones. Rock Mech. Rock Eng. 54, 129–148. https://doi.org/10.1007/s00603-020-02248-3.
Wang, R., Gu, Y.J., Schultz, R., Chen, Y., 2018. Faults and non-double-couple components for induced earthquakes. Geophys. Res. Lett. 45, 8966–8975. https://doi.org/10.1029/2018GL079027.
Wesnousky, S.G., 1988. Seismological and structural evolution of strike-slip faults. Nature 335. https://doi.org/10.1038/335340a0.
Wiemer, S., Wyss, M., 2002. Mapping spatial variability of the frequency-magnitude distribution of earthquakes. G. In: Dmowska, R., Saltzman, B.B.T.A. (Eds.), Advances in Geophysics. Elsevier, p. 259. https://doi.org/10.1016/S0065-2687(02)80007-3. V.
Wiemer, S., Wyss, M., 1997. Mapping the frequency-magnitude distribution in asperities: an improved technique to calculate recurrence times? J. Geophys. Res. Solid Earth 102, 15115–15128. https://doi.org/10.1029/97JB00726.
Zang, A., Christian Wagner, F., Stanchits, S., Dresen, G., Andresen, R., Haidekker, M.A., 1998. Source analysis of acoustic emissions in Aue granite cores under symmetric and asymmetric compressive loads. Geophys. J. Int. 135, 1113–1130. https://doi.org/10.1046/j.1365-246X.1998.00706.x.
Zhang, H., Eaton, D.W., Li, G., Liu, Y., Harrington, R.M., 2016. Discriminating induced seismicity from natural earthquakes using moment tensors and source spectra. J. Geophys. Res. Solid Earth 121, 972–993. https://doi.org/10.1002/2015JB012603.
Zielke, O., Galis, M., Mai, P.M., 2017. Fault roughness and strength heterogeneity control earthquake size and stress drop. Geophys. Res. Lett. 44, 777–783. https://doi.org/10.1002/2016GL071700.